

Intensified paraglacial slope failures due to accelerating downwasting of a temperate glacier in Mt. Gongga, Southeastern Tibet Plateau

Yan Zhong^{1,2}, Qiao Liu¹, Matthew Westoby³, Yong Nie¹, Francesca Pellicciotti⁴, Bo Zhang⁵, Jialun Cai⁵, Guoxiang Liu⁵, Haijun Liao^{1,2}, Xuyang Lu¹

- 5 ¹ Institute of Mountain Hazards and Environment, Chinese Academy of Sciences, Chengdu 610041, China
² College of Resources and Environment, University of Chinese Academy of Sciences, Beijing 100049, China
³ Department of Geography and Environmental Sciences, Engineering and Environment, Northumbria University, Newcastle upon Tyne NE1 8ST, UK
⁴ Swiss Federal Institute for Forest, Snow and Landscape Research WSL, 8903 Birmensdorf, Switzerland
10 ⁵ Department of Surveying and Geo-Informatics, Faculty of Geosciences and Environmental Engineering, Southwest Jiaotong University, Chengdu 611756, China

Correspondence to: Qiao Liu (liuqiao@imde.ac.cn)

Abstract. Topographic development via paraglacial slope failure (PSF) represents a complex interplay between geological structure, climate, and glacial denudation. Southeastern Tibet has experienced amongst the highest rates of ice mass loss in High Mountain Asia in recent decades, but few studies have focused on the implications of this mass loss on the stability of paraglacial slopes. We used repeat satellite- and UAV-derived imagery between 1990 and 2020 as the basis for mapping PSFs from slopes adjacent to Hailuoguo Glacier (HLG), a 5 km-long monsoon temperate valley glacier in the Mt. Gongga region. We observed recent lowering of the glacier surface at rates of up to 0.88 m a⁻¹ in the period 2000 to 2016 whilst overall paraglacial bare ground area (PBGA) on glacier-adjacent slopes increased from 0.31±0.27 km² in 1990 to 1.38±0.06 km² in 2020. Decadal PBGA expansion rates were ~0.01 km² a⁻¹, 0.02 km² a⁻¹ and 0.08 km² in the periods 1990-2000, 2000-2011, and 2011-2020 respectively, indicating an increasing rate of expansion of PBGA. Three types of PSF, including rockfalls, sediment-mantled slope slides, and headward gully erosion, were mapped, with a total area of ~~XX km²~~. We observed recent lowering of the glacier surface at rates of up to XX m a⁻¹ in the period XXXX–XXXX whilst overall paraglacial bare ground area (PBGA) on glacier adjacent slopes increased from 0.31±0.27 km² in 1990 to 1.38±0.06 km² in 2020. Total PBGA area increased from XX±XX km² in 1990 to 0.75±0.03 km² in 2020. Decadal PBGA expansion rates were 0.01 km² a⁻¹, 0.02 km² a⁻¹ and 0.08 km² in the periods 1990–2000, 2000–2011, and 2011–2020 respectively, indicating an increasing rate of expansion of PBGA. South-facing valley slopes (true left of the glacier) exhibited more destabilization (56% of the total PSFs area) than north-facing (true right) valley slopes (44% of the total PSFs area). Deformation of sediment-mantled moraine slopes (mean 1.65–2.63–1.6–2.6±0.04 cm d⁻¹) and an increase in erosion activity in ice-marginal tributary valleys caused by a drop in local base level (gully headward erosion rates are 0.76–3.39 cm d⁻¹) have occurred in tandem with recent glacier downwasting. We also observe deformation of glacier ice, possibly driven by destabilisation of lateral moraine, as has been reported in other deglaciating mountain glacier catchments. ~~We hypothesize that~~ the formation, evolution, and future trajectory of PSFs at HLG Hailuoguo Glacier (as well as other monsoon-dominated deglaciating mountain areas) are related to glacial history.

35

including recent rapid downwasting leading to the exposure of steep, unstable bedrock and moraine slopes, and climatic conditions that promote slope instability, such as very high seasonal precipitation and seasonal temperature fluctuations that are conducive to freeze-thaw and ice segregation processes.

Abstract. Topographic development via paraglacial slope failure (PSF) represents a complex interplay between geological structure, climate, and glacial denudation. Where debris generated by PSFs is deposited on the surface of a glacier, this debris can increase the extent or thickness of a supraglacial debris cover, in turn modifying glacier ablation and affecting meltwater generation. Southeastern Tibet To date, This study pays little attention has been paid to the intensity and frequency of PSFs in glacierised, monsoon temperate regions of Southeast Tibet, a region has experienced the most amongst the highest rates remarkable accelerating of ice mass loss in among High Mountain Asia during in recent decades, but few studies have focused on the implications of this mass loss on the stability of paraglacial slopes.past decades. In this case, WwWe used repeat satellite and UAV derived imagery between 1990 and 2020 as the basis for mapping PSFs from slopes adjacent to along

40 the 5 km long, 0.5 km width, west east trending ice tongue of Hailuoguo Glacier (HLG), a 5 km long, well monitored monsoon temperate valley glacier in the Mt. Gongga region, using repeat satellite and UAV derived imagery between 1990 and 2020. Three types of PSF, including rockfalls, sediment mantled slope slides, and headward gully erosion, were mapped. Our study period saw lowering of the glacier surface at rates of up to XX m a⁻¹, Accompanying with the observed glacier retreat and thinning, whilst the overall paraglacial bare ground area (PBGA) on glacier adjacent slopes increased from

45 0.31±0.27 km² in 1990 (Landsat TM) to 1.38±0.06 km² in 2020 (PlanetScope). Total PBGA area increased from XX±XX km² in 1990 to 0.75±0.03 km² in 2020. with dDecadal PBGA expansion rates were rates from -0.01 km²·a⁻¹ in 1990-2000, and 0.02 km²·a⁻¹ and 0.08 km² in the periods 1990-2000in, 2000-2011, to and 0.08 km²·a⁻¹ in 2011-2020 respectively, indicating an increasing rate of expansion of PBGA.an intensified paraglacial failure process. Three types of PSF were identified: (A), including (A) rock fallrockfall, (B) (B) sediment mantled slopes slide and collapse, and (C) (C) gully headwards erosion, with

50 a total area of 0.75±0.03 km² in 2020, were identified and documented based on recently repeat high resolution UAV mappings, with a total area of 0.74±0.03 km² in 2020. We analysed tThe formation, evolution, and current state status of these typical PSFs and discuss these aspects with relationare generally related to the interconnected history of glacier extent and dynamics and paraglacial geomorphological historyadjustments, and also likely influenced modulated and/or disturbed by the fluctuations of in air temperature/ and precipitation and their combinations; the latter is . Despite a slightly decreasing trend of

55 annual precipitation was observed at our studied site, the absolute high amount precipitation in Mt. Gongga as well as other monsoon dominated deglaciating mountain areas must has played important roles in the intensified denudation, nested processes and failure of the paraglacial slopes. REVISIT. South facing slopes (true left of HLG) showed more destabilization (56% of total PSFs area) and higher PSF activity than north facing slopes (44% of total PSFs area). We observed annual average rates of downslope sliding for type B PSFs of 1.6-2.6±0.04 cm d⁻¹, whereas the average upward denudation rate for type C PSFs was 0.7-3.39±0.31 cm d⁻¹. We show that type A PSFs are non ice contact rock fallscollapses that occur as a long-term paraglacial response following glacier downwasting and the exposure of steep rocky cliffs and which could also be influenced by precipitation, freeze-thaw cycling, earthquakes or other factors. In contrast, type B and C PSFs isare a more immediate response to recent glacier downwasting. We further argue that the accelerating downwasting of glacier are used as a preparatory or triggering factor, which could directly or indirectly cause the PSFs. We also found some unstable slopes in

60 the lower slope angle areas which may be related to the slope material and the failure process.

65

70

1 Introduction

The thinning and retreat of mountain glaciers exposes new, unstable landscapes which are susceptible to rapid geomorphological changes (i.e., with a high entropy). Sparsely vegetated or unvegetated drift-mantled slopes are particularly susceptible to ~~be modified~~ modification by gravitational, aeolian and fluvial processes and can be rapidly reworked by debris flows, rock avalanches and slope-wash (Ballantyne, 2002~~3~~; Ballantyne, 2003~~2~~; Deline et al., 2015a; Eichel et al., 2013). Glacier downwasting can destabilize slopes through undercutting, ~~and -and, simultaneously, the progressive reductions in loss of buttress exerted by ice loading on its adjacent slopes (debuitressing) of ice-marginal slopes can may~~ result in rock stress ~~-release and, in turn, instability. The observed permafrost degradation is also exacerbating these local changes in topographic~~ (Gruber et al., 2017), ~~s, scilicet “debuitressing”, altering the state of stress that exists within the slope accordingly. The Such~~ slope failures initiate ~~fourive predominant possible~~ modes of slope response in deglaciating catchments are: (1) large-scale catastrophic rock slides and rock avalanches (Kirkbride and Deline, 2018; Fischer et al., 2010); (2) ice-contact slope movements (McColl and Davies, 2013); ~~and~~ (3) periodic small-scale rock topples or ~~rock fall~~ rockfalls (Cook et al., 2013); ~~(4) and (4)~~ deep-seated gravitational creep (Deline et al., 2015b; Ballantyne et al., 2014), ~~and (5) paraglacial debris cones and valley fills (Ballantyne, 2002).~~ These ~~fourive types of r~~esponses provide a useful framework for examining the processes and geomorphological consequences of slope adjustment ~~during or following after~~ deglaciation. These responses can be further divided into two types: *rock slope failures* and *sediment slope failures*, which ~~are usually~~ can be described collectively as *paraglacial slope failures* (PSFs). PSFs encompass failure of steep rock walls and lateral moraine slopes following glacier downwasting (Church and Ryder, 1972; Fickert and Grüniger, 2018) and are widely distributed in deglaciating or deglaciating landscapes.

PSFs constitute a key mechanism for rapid degradation of recently glacial landscapes, as they contribute to the disaggregation of large portions of valley sides and the transformation from U-shaped to V-shaped valleys. ~~High frequency, low magnitude~~ PSFs can transport a considerable volume of debris onto glacier surfaces (Smith et al., 2020), thereby ~~facilitate~~ ing the accumulation of the supraglacial moraine. ~~More recently, a study in the Himalaya measured the sediment from lateral moraines increasing in debris thickness (sediment slope failures) by 0.08 m a⁻¹ of the glacier surface (van Woerkom et al., 2019). The rocks and debris from a catastrophic rock avalanche (rock slope failures) in southeast Tibet covered the entire glacier surface and the wider area around and downstream (Kääb et al., 2021). They (lateral moraine and bordering rock walls) encompass two of the three potential sources of supraglacial debris (the other is basal erosion, (Reheis, 1975; Boulton, 1978)).~~ Because thin debris covers enhance ablation, whilst thicker covers suppress it (Fyffe et al., 2020), debris supply dynamics ultimately affect ~~the~~ glacial ablation and meltwater production (Rowan et al., 2018). ~~In addition, accompanied by relatively rare but oecasional rain storm events, those unsorted debris deposited by PSFs can be (re) are very likely transformed mobilised into debris-mass flows and other eaeading geo-disasters-hazard cascades that threaten-directly threaten human life, property, and infrastructure, downstream infrastructure, and can affect freshwater availability quality and the safety of residents and tourist~~

(Hewitt et al., 2011; Reznichenko et al., 2012). A high-profile example is the 2021 Chamoli mass flow, northern India, that was the rock-ice avalanches transformed into a catastrophic debris flow, causing the destruction of two hydropower projects and more than 200 casualties (Shugar et al., 2021).

Monsoonal temperate glaciers in the Southeastern (SE) Tibetan Plateau (SETP) have experienced higher rates of mass loss and ice thinning compared to other High Mountain Asia (HMA) glacierized regions in High Mountain Asia (HMA) in past decades (Neckel et al., 2017; Brun et al., 2017), with an average thinning rate of $-0.55 \pm 0.23 \text{ m a}^{-1}$ during 2000 to 2016 (Brun et al., 2017). In addition to being seismically active, the combination of a large amount of high-intensive rates of glacial meltwater ablation and abundant extremely monsoonal precipitation during the summer monsoon and steep topography makes the SE-Tibet highly one of the most susceptible regions to offer cryospheric glacier or water related geo-hazards (Yao et al., 2019a), such as glacial debris flows, ice/snow avalanches, glacier-related landslides, and glacial lake outburst floods (Fan et al., 2019; Cheng et al., 2010; Xu et al., 2012). Further for example, a total of at least four glacier-related landslides (1990-2018, (Liu et al., 2010; He et al., 2008; Pan et al., 2012; Cao et al., 2019; Liu et al., 2018; Liu and Liu, 2010)), and twelve 12 glacial lake outburst floods (1931-2014, (Liu et al., 2019b; Yao et al., 2014)) incidents have been recorded across the SETP, and it has been suggested that more than half of the debris flows recorded in the SETP were cryogenic (Hu et al., 2011). ~~Tibetan Plateau. Mass movements resulting from large-scale slope failures routinely form temporary valley-blocking natural dams (Liu et al., 2019c), behind which large lakes can develop and eventually outburst. Glacier destabilization itself was also one of the concerned sources of cascade hazard event, such as historically reported surge induced catastrophes (Zhang, 1985) and recent ice avalanche induced debris flow that blocks the Yarlung Tsangpo river (Chen et al., 2020; Käab et al., 2021). Mass movements originating from tributary valleys where glacier recession and permafrost thaw has reduced slope stability has likely contributed to the availability of debris that can be incorporated into mass flows these large scale slope failures (Zou et al., 2020; Korup et al., 2010). The region also has a history of gFor example, mIt was also suggested that more than half of the debris flows recorded in the Linzhi Area, SE Tibet, SETP can be sourced to a were cryospheric trigger (Hu et al., 2011). Further, a total of four glacier related landslides (1990-2018, (Liu et al., 2010; He et al., 2008; Pan et al., 2012; Cao et al., 2019; Liu et al., 2018; Liu and Liu, 2010)), and twelve glacial lake outburst floods (1931-2014, (Liu et al., 2019b; Yao et al., 2014)) incidents have been recorded across the SE Tibetan Plateau. These hazards have caused severe economic losses and heavy casualties and have affected socioeconomic development. Glacier destabilization and detachments itself was also one of the concerned sources of cascade hazard event, such as historically reported surge induced catastrophes (Zhang, 1985) and the detachment of the tongue of Sedongpu Glacier, which triggered a debris flow that recent ice avalanche induced debris flow that temporarily blocked the Yarlung Tsangpo river (Chen et al., 2020; Käab et al., 2021). These cascading geo-hazards have caused severe economic losses or some heavy casualties to SETP local communities.~~

With populations and economies expanding, and it -

140 ~~With populations and economies expanding, it is anticipated that the magnitude and frequency of glacier related cryospheric hazards in the SETP will increase in near future (Yao et al., 2019b) since the accelerating glacial mass loss and permafrost degradation due to climate warming will continue to destabilize the paraglacial landscapes (McColl, 2012). Since the accelerating glacial mass loss and permafrost degradation due to climate warming will continue to destabilize the paraglacial landscapes (McColl, 2012). It is anticipated that accelerating glacial mass loss and permafrost degradation due to climate warming will continue to destabilize the paraglacial landscapes and thus increase the frequency of related hazards in the SE Tibet Plateau.~~

145
150 Mt. Gongga is located on the southeastern edge of the Tibetan Plateau, in the geological transitional zone between the Plateau and the Sichuan Basin (Liu and Zhang, 2017). It is a large natural reserve with medium human disturbance and a relatively developed glacier tourism sector. According to the Second Glacier Inventory in China (Liu et al., 2015), there are 75 temperate glaciers in Mt. Gongga, of which five larger valley glaciers have a length >10 km, including Hailuoguo Glacier, Mozigou Glacier, Yanzigou Glacier and Nanmenguangou Glacier on the eastern slope, and Gongba Glacier on the western slope (Li et al., 2010). In recent decades, remarkable retreat and thinning of these glaciers has been widely reported (Liu et al., 2010; He et al., 2008; Pan et al., 2012; Cao et al., 2019; Liu et al., 2018; Liu and Liu, 2010) and catastrophic glacial geomorphological processes or glacier related hazards, such as glacial debris flows and landslides, occur frequently in the Mt. Gongga region (Xu et al., 2007; Cai et al., 2021). PSFs in these catchments are generally considered to occur on steep rocky terrain and manifest as mixed ice/snow/rock avalanche and rockfall originating from surrounding walls and triggered by frost weathering processes. Most glaciers on Mt. Gongga have a considerable surface debris cover in their ablation zones and are bordered by unconsolidated lateral terminal moraines in the periglacial zones.

160 ~~While a growing body of work research studies focuses on the destabilization of the process of paraglacial hillslopes destabilization of in the European Alpine (Curry et al., 2006; Kirkbride and Deline, 2018) and Southern Alps (Cody et al., 2020; McColl, 2012), and Cordillera Blanca (Andes) (Emmer et al., 2020) and Central Himalayas (van Woerkom et al., 2019), these studies which have reported more on slope monitoring. Although they have recorded the glacier retreat and thinning and listed it as the main factor of slope instability, case studies combining the monitoring of multi-dynamic of glaciers and paraglacial slope and reporting for the transient condition of paraglacial slopes in the deglaciating monsoonal temperate glaciers in SETP are clearly lacking. We hypothesize that glacier dynamic change, including retreat, downwasting, and slowing, can explain the (prone to) instability of paraglacial slope. Meanwhile, in the monsoon-dominated temperate glacier regions, a climate of warm-wet synchronization is the primary precondition driving the paraglacial rock and sediment slope failure.~~

170 ~~To this end, yet very few cases studies focus on have been reported for the transient condition of the analysis of paraglacial slopes in the deglaciating To addresses In study we select the Hailuoguo Glacier (HLG, a monsoon temperate glacier in Mt.~~

Gongga that has been well documented and observed since the early 20th century) as a detailed case site to study the interactions between glacier shrinkage and paraglacial (rock and sediment) slope adjustments during the past decades. focus on the monsoon temperate the), located in , monsoon in the Mt. Gongga region) as casesite to studyon the interactions between shrinkage and paraglacial adjustmentduring the past decades. We combine visual

In this study we carried out investigations on the PSFs processes of Hailuogou Glacier (HLG) a typical temperate glacier located on the east slope of Mt. Gongga. Our investigations are based on the analysis of historical satellite imageryimagerys and recent field based imagery high resolution the field phototopography mappings usingimagery acquired from an acquired from an unpiloted aerial vehicle (UAV), combined with on-siteu geomorphological observations and measurements. The main objectives of this research are to:

C. (iA) map and quantify the spatiotemporal variability of PSFs map and quantify slope failures and topographic change around the lower tongue of HLG Hailuogou Glacier through based on time-time-series image comparison; (iiB) .To explain the spatiotemporal variability of PSFs.;

D. Cclassify the PSFs, analyse their topographic conditionsdescribe and discuss the spatial distribution, spatiotemporal evolution, and discuss their possible forcing-physical mechanisms in monsoon-dominated temperate glacier regions of different types of PSFs. To explain the paraglacial slope evolution and sediment delivery processes.;

E. (iiiC) discuss the geomorphic and environmental effects of these slope processes. To by explaining the and further discuss possible linkages between PSFs, climate change, and glacier downwasting and- PSFs in a typical monsoon dominated region characterised by as accelerated glacial and paraglacial denudation.

2 Study area

HLG Hailuogou Glacier (29°58.4'N, 101°91.6'E) is one of the largest debris-covered valley glaciers in the Mt. Gongga region (Fig. 1). It is a ~13 km-long, east-facing monsoon temperate glacier, has an area of 24.7 km², and extends in altitude from 2990 m to 7556 m a.s.l. The glacier is ~300-500 m in width, and the wider valley is deeply incised below the accumulation area, (where the glacier broadens to ~6 km in width). The upper section of the ice tongue (below the icefall) has a surface gradient of ~10° and is connected to very steep (~55°) lateral slopes on both sides. At a distance of ~1.5 km from the base of the icefall (middle section of the ice tongue); the glacier surface steepens to ~12° and becomes highly crevassed. At a distance of 2 km, the glacier turns its flow direction toward the north-east, and maintains a surface gradient of ~13° for the remaining 3 km (lower section of the ice tongue) stretching to the Little Ice Age (LIA)-end of the glacier tongue-moraine. Paralleling with the lower section of the ice tongue, the height of lateral moraines to the current glacier surface is about 165 m, which is comparatively higher than the further upper glacier (~86 m at the middle section of ice tongue).

The terminus of HLG has retreated more than 2 km since the LIA (Su and Shi, 2002) and this retreat has accelerated from 12.7 m a⁻¹ between 1966–1989 to 27.4 m a⁻¹ between 1998–2008. Between 1966 and 2009, the mean ice surface elevation of its

205 lower tongue had lowered at a rate of $1.1 \pm 0.4 \text{ m a}^{-1}$ (Zhang et al., 2010). Due to a suitable local thermal (warm) and moisture
forelands and lateral moraine slopes, and even on some supraglacial debris-covered areas that are largely stagnant. The LIA
preglacial zone (2980-2800 m) is characterized by extremely fast primary vegetation succession, and hosts an integrated
community ranging from cold-adapted herbaceous species to *Abies fabri* (conifer pine) forest. *Abies fabri* forest patches are
also seen along both lateral sides of the ice tongue on the accumulated lateral moraine, which has been relatively stable since
210 the LIA.

Due to its low altitude, easy accessibility, and adjacency to the forests and hot springs, HLG and its surrounding areas have
been exploited for tourism since 1987. A glacier ropeway connects the two lateral moraines and transports visitors across the
lower part of the ice tongue and provides access to a viewpoint on the southern side of the valley (S2 on Fig. 1) from where
215 the ice tongue can be overlooked and accessed via trail. Between 2000 and 2011, the number of annual visitors increased from
44,000 to 384,000 (Zhu, 2015), and in 2019 the number reached ~2,852,600 (Haiguanju, 2020). The increasing popularity of
the glacier comes at a time when tourism facilities and infrastructure are becoming frequently disturbed due to paraglacial
landsliding/landslides, debris flows, and flash floods (Xu et al., 2007; Cai et al., 2021). Beyond the objectives outlined above,
there is a need to more fully understand the nature of slope failures in the vicinity so that these failures might be better
220 anticipated, and their potential impacts mitigated where possible.

3 Data and methods

3.1 Paraglacial slope failures (Paraglacial Slope Failures) mapping and classification

225 Given a warm and humid climate condition, vegetation colonisation of newly exposed bare ground is very fast (1-2 years)
in the the HLG paraglacial environment/catchment. Since Like many monsoonal temperate glaciers in SETP, the lower part
of the HLG tongue and its adjacent slopes are located below the local tree line, and so areas of new bare ground caused by
slope destabilisation are relatively easy to detect; we call these areas any newly developed PSFs could be readily recognized
from the changed paraglacial exposed bare ground area (PEBGA). To map the extents of PSFs for addressing objective A, Due
to the strong influence of the monsoon, the HLG is often covered with thick clouds in summer, rendering 75% of the available
230 historical summer satellite image archives unusable. However, we successfully screened and synthesized several Landsat or
Sentinel-2 cloudless images in 1990, 2000, 2016, and 2018 using the Google Earth Engine platform. A total of 8 satellite
images acquired between 1990 and 2020 (Table 1) including Sentinel-2 (10m), RapidEye (5m), PlanetScope (3m), were used
to extract the PSFs. We firstly we extracted the paraglacial PEBGA non-vegetated areas by classifying the land surface as with
vegetated or and unvegetated areas using with the using the Normalized Difference Vegetation Index (NDVI), which was
235 derived calculated using reflected red and near-infrared band values of satellite images. Shadows caused by the relative angle
between the sun, ground objects, and sensors will reduce the value of NDVI, but by adjusting the threshold, the vegetated and

non-vegetated areas can still be differentiated. Therefore, we used cloudless images in multiple seasons (spring, autumn, and summer) to automatically extract -PSFs boundaries. Of the seasonal data, the PSF boundaries extracted from images acquired in the northern hemisphere summer generally suffered less from the terrain shadow than other seasons and can be used directly after validation, and the boundaries extracted from other seasons need to be manually corrected. The PBGAsPSFs were then extracted by excluding the glacier-covered areas covered by the glacier extents (GCAs) to generate an initial mapping of PSF. Some areas of PBGA showed an interannual change or a sudden change in visual shape. However, due to the climate conditions, vegetation colonisation is extremely fast in HLG environment. For better inter-annual comparisons, we then manually removed those patches and areas where the PBGA had changed due to vegetation colonisation in some paraglacial slopes and in all glacier foreland, some changed PBGA caused by vegetation colonisation which, mainly in the glacier foreland, were manually removed. Finally, those to keep the remaining unstable slope areas were final mapped as PSFs. A total of 8 satellite images between 1990 and 2020 (Table 1), including Sentinel 2 (10m), RapidEye (5m), PlanetScope (PL, 3m), were used to extract the PSFs. These data constitute a multi temporal and dynamic observation of HLG and its surrounding paraglacial environments. Due to the strong influence of the monsoon, the HLG is often covered with thick clouds in summer, rendering 75% of the available summer satellite images unusable. However, we successfully screened and synthesized several Landsat or Sentinel 2 cloudless images in 1990, 2000, 2016, and 2018 using the Google Earth Engine platform. Shadows caused by the relative angle between the sun, ground objects, and sensors will reduce the value of NDVI, but by adjusting the threshold, the vegetated and non-vegetated areas can still be differentiated. extracted NDVI can eliminate a part of the effect of hill shade caused by the low angle of the sun on ground recognition. Therefore, we can use cloudless images of in multiple seasons (spring, autumn, and summer) to realize automatic extraction of PSFs boundaries. Of the seasonal data, the PSF boundaries extracted from images acquired in the northern hemisphere summer are generally suffered less from the terrain shadow than other seasons and can be used directly after validation, and the boundaries extracted from other seasons need to be manually corrected partly. According to the principles of systematization, standardization, operability and scalability, the PSF are classified combining the knowledge of the basic slope material composition, erosion type, visual shape, and event magnitude obtained from field investigation and UAV data in HLG, and the classifications proposed by Ballantyne (2002), McColl (2012), Jarman (2006), and Hungr et al. (2014). A classification standard for PSF systems is proposed, which is divided into two major categories: rock slope failure and sediment slope failure; and five sub-categories: rock avalanches, rockfall, deep-seated gravitational slope deformations, sediment-mantled slope slide, and gully headward erosion (Tab. S1).

To enable more detailed mapping of recent PSF extents, UAV sorties were flown on 31 August 2016, 07 June 2017, and 15 May 2019 using a DJI Phantom 4 Pro UAV, and 19 August 2018 using a DJI Phantom 4 RTK UAV, which combination of a global navigation satellite system (GNSS) with a mean horizontal accuracy quality of $0.01\text{ m} + 1\text{ ppm}^*$ (RMS) in XY (<https://www.dji.com/uk/phantom-4-rtk/info#specs>), and iAerial nput photographs were co-aligned stitched using Structure

* 1 ppm means the error has a 1mm increase for every 1 km of movement from the aircraft/drone.

from Motion (SfM) software ContextCapture Center Master (version 4.2) to create a time series of orthomosaic aerial images at 0.1m resolution, and with a mean RMS error of $0.01 \text{ m} + 1 \text{ ppm}^\dagger$ (RMS) in XY. However, some of our earlier UAV surveys were routed with included limited coverage area of off-glacier terrain that it was less effectively mapped by photograph overlapping (i.e., Section 3.2), and so we could not map PSFs on all ice-marginal slopes. This design aspect of the UAV surveys, combined with steeply topographic constraints on the UAV flight area, meant that not all ice-marginal slopes were successfully mapped on the final orthomosaics as well as for the later UAV surveys (Fig. S1). To enable co-registration of UAV images with satellite imagery, we selected 54 features (e.g., exposed bedrock, trees, or building vertices) from stable ground areas (Fig. S1) for use as ground control points (GCP) and which were identifiable on both PlanetScope and UAV images. The altitude (z) of each GCP was then extracted from the ALOS PALSAR DEM. The final mean (and maximum) RMS error of the GCPs was 1.22 (1.98) pixels, equating to a mean xy horizontal error of 0.15 m. An additional error of ± 0.5 pixels was estimated to include all the uncertainties of visual interpretation and automatically extracted areas (i.e. multiply linear error and perimeter, e.g. the linear error of Landsat images are 15m, Sentinel 2 images 5 m and PlanetScope images ~ 1.56 m) (Salerno et al., 2012; Haritashya et al., 2018). Our workflow is summarized in Fig. 2. All UAV images are co-registered using an orthorectified PL image acquired on 16 August 2018, which was found to be perfectly co-registered with a 12.5m hillshade of ALOS PALSAR DEM when manually comparing their topography textures (e.g., terrain ridges and vertices) from the peak of Mt. Gongga (7556 m a.s.l.) to the trimlines of the glacier close to its terminus (~ 3000 m a.s.l.). To execute the UAV images co-registration, a total number of 54 features (Fig. S1) were selected as ground control points on stable ground surfaces (e.g., exposed bed rock, trees, and or some building vertices) around the ice tongue on the both PL image and UAV images, and their corresponding altitudes were then extracted from the ALOS PALSAR DEM. Finally, overall, the final reported quality of the co-registered UAV images successfully occupied positions were quite satisfactory (with a total and (maximum) RMS error of: 1.22 and (1.98) pixel respectively, from which the calculated i.e. a mean horizontal quality in XY is error of 0.15 m in XY).

Additionally, an additional error of ± 0.5 pixels was estimated to include all the uncertainties of visual interpretation and automatically extracted areas (i.e. multiply linear error and perimeter, e.g. the linear error of Landsat images are 15m, Sentinel 2 images are 5 m, and of PlanetScope images are ~ 1.56 m) (Salerno et al., 2012; Haritashya et al., 2018). Our workflow is summarized in Fig. 2.

According to the principles of systematization, standardization, operability and scalability, the PSF are classified combining the knowledge of the basic slope material composition, erosion type, visual shape, and event magnitude obtained from field investigation and UAV data in HLG, and the classifications proposed by Ballantyne (2002), McColl (2012), Jarman (2006),

[†] 1 ppm means the error has a 1mm increase for every 1 km of movement from the drone.

300 ~~and Hungr et al. (2014). A classification standard for PSF systems is proposed, which is divided into two major categories: rock slope failure and sediment slope failure; and five sub categories: rock avalanches, rock fall/rockfall, deep seated gravitational slope deformations, sediment mantled slope slide, and gully headward erosion (Tab. S1).~~

~~3.3.2 Slope movement and outline change~~headscarp erosion rates

305 ~~To quantify the rate of slope surface displacement speed of slopes movement between 2016 and 2020 for address objective A, we selected 20-40 points as (trackable features used QGIS software to identify between 20-40 feature tie points that were located on easily trackable features including such as of large rocks, paths, or infrastructures) discolouration areas on a series of UAV-mapped slopes (B1-B4 in Fig. S2, Fig. S3).~~ We manually tracked the ~~location displacement~~ of each point in the QGIS software and calculated their mean annual horizontal displacements annually. ~~For areas exhibiting no discernible in~~
310 ~~some~~ ~~For cases that, the displacement movement of the slope movement, itself is unapparent less notability or extremely low, but where we observed headscarp erosion of slope instabilities the headward backwasting these same slopes have is detectable significant headscarp erosion. To, we quantifiedy their this rates of headscarp erosion, we. Based on used the PSF boundaries outlined by delineated on five higher- resolution remote sensing satellite images from 2002 to 2019 (Google Earth SPOT-5 imagery for 2002, RapidEye images for 2011, 2014, and 2015, and PlanetScope image for 2019), towe calculated~~
315 ~~at the mean distance and annual retreat rates for these headscarps viausing the QGIS Average Nearest Neighbor/Neighbour Analysis procedure.~~

~~3.3.2 Glacier dynamics observations~~

~~Since~~ ~~Because~~ ~~The evolution of paraglacial slopes and their topographic conditions are is closely related to the glacier dynamics (Ballantyne and Benn, 1994; Ballantyne, 2002). It is not only related to the area and thickness of the glacier, but~~
320 ~~also to the speed of its movement. As the glacier moves, both sides of the slope erode and some of the sediment that has accumulated at the foot of the slope is carried away (Egholm et al., 2011). Furthermore, they corroborate each other (Neckel et al., 2017). On the one hand, the thinning of the glacier slows down the glacier moves; on the other hand, when the glacier slows down, the ice flux transported is reduced, which accelerates the glacier thinning and ultimately leads to the slope sliding. Therefore, we thus analysed the geomorphological processes and implications of retreat, thinning and~~
325 ~~slowdown of the HLG and their relationships with the PSFs development to address objective B, the changes of the glacier elevation and velocity were analysed.~~

~~Many scholars have done Detailed research mapping of in the area changes retreat and thinning of the HLG over the past years decades has been well documented and reported (Li et al., 2010; He et al., 2008; Liu et al., 2018; Zhang et al., 2010; Liu et al.,~~
330 ~~2010). We extend the boundary of G glacier terminus retreat history was extended to 2020/19 using some newly archived satellite images used in this study (Fig. 1 and Table 1). Zhang et al. (2010) reported a mean surface lowering rate of 1.1 ± 0.4 m~~

~~a⁻¹ between 1966 and 2009 for the lower part of HLG ice tongue. Using hydrological balance approach, Liu et al. (2010) estimated a thinning rate of 0.5±0.4 to 0.7±0.4m a⁻¹ (1994–2004) for the whole HLG area. A more recent investigation by Cao et al. (2019) updated the period to 2015 and gave an overall mean ice surface lowering rate of 0.54±0.04m a⁻¹ for all glaciers in Mt. Gongga. In this study, we compile above results and extended it to 2016 following Brun et al. (2017), who published a regional dataset of glacier surface elevation changes for the High Mountain Asia derived by differencing ASTER DEMs between 2000 and 2016. We employed the TopoDEM (1966) reported by Zhang et al. (2010), the Shuttle Radar Topography Mission (SRTM, 2000) 30m DEM (Farr et al., 2007), and then calculated 2016 DEM calculated using based on the 2000–2016 the glacier mean annual surface elevation change s between 2000 and 2016 for the High Mountain Asia published rate by from Brun et al. (2017) ASTER DEM difference between 2000 and 2016 to analyse the surface elevation changes of HLG between 1966 and 2016. Surface elevation changes along five profile-lines in longitudinal (A-A' ~~is~~ along the glacier central flow line) and transverse (B-B', C-C', D-D' and E-E' perpendicular to the glacier central flow line) on the lower part of HLG (Fig. 1) were examined and compared. The four transverse lines intersected were examined approximately cover along the every three types of PSFs (definition below in Section 4.2) and a sufficient distance is maintained in each transverse profile for comparison. Glacier terminus retreat history was extended to 2019 using satellite images used in this study (Fig. 1).~~

For ice flow dynamics, the earliest observations of surface velocity of the HLG were during 1982–1991 field expeditions, during which the location changes of several stakes along the ice tongue were repeatedly measured. Unfortunately, the original coordinates data of those measurements (e.g., the precise geographic locations of the stakes) was not offered and results are published only as a velocity isoline map with point velocity value indicated. Zhang et al. (2010) has reported a multi-decadal slowdown of the HLG ice tongue between 1980s, 1990 and 2008, when an updated stake-based ice velocity was conducted during the 2008 summer. Using 38 SAR images acquired by PALSAR-1/2 satellites from 2007 to 2018, Liu et al. (2019a) extracted annual surface displacement velocities of the HLG between 2007 and 2018. Here we compared the long-term ice flow velocity changes of the HLG (also checked along the five profile-lines mentioned above), based on three-periods results of 1982–1983 (in situ observed; the scanned picture of HLG velocity between 1982 and 1983 is in Fig. S4), 2007–2011 and 2014–2018. The velocity in 1982–1983 is based on a published velocity map (scanned and shown in Fig. S4), which were derived via calculated and extrapolating from of in-situ measurements of stake locations acquired using total station. Glacier surface The velocities for the period during 2007–2011 and 2014–2018 were derived from ALOS/PAL(SAR satellites using derived feature tracking method by offered by Liu et al. (2019a)).

~~3.3 Slope movement and outline change rate~~

~~To quantify the surface displacement speed of slopes, we used QGIS software to identify between 20–40 tie points on a series of slopes (B1–B4 in Fig. 6, Fig. S2). We manually tracked the displacement of each point and calculated the mean horizontal displacement. In some cases, the displacement of the slope itself is unapparent or extremely low, but these same slopes have detectable headscarp erosion. To quantify rates of headscarp erosion, we used the PSF boundaries outlined by five high-~~

365 ~~resolution remote sensing images from 2002 to 2019 (Google Earth SPOT-5 imagery for 2002, RapidEye images for 2011, 2014 and 2015, and PlanetScope image for 2019) to calculate a mean distance and annual retreat rate for these headscarps.~~

3.4 Meteorological data

370 ~~Meteorological conditions nearby the HLG were diagnosed ~~To discuss their possible forcing mechanisms and/or the climate change effect of impacts on the development of PSFs for address the objective B and C. The d~~Daily air temperature and precipitation data (1988/01/01--2018/12/31) ~~were used in this study were sourced from~~observed by the Subalpine Ecosystem Observation Station (3000 m a.s.l., 2 km from glacier terminus), and provided by the Gongga Alpine Ecosystem Observation and Experiment Station (Gongga Mt. Station, 3000 m a.s.l., 2 km to the glacier terminus) with a standard automatic weather station (AWS), ~~installed and managed by the~~ Chinese Ecological Research Network (CERN; <http://www.cern.ac.cn/>). ~~We also obtain~~collected the manually observed daily temperature data (observed at 2:00 am, 8:00 am, 2:00 pm, 8:00 pm every day) 375 ~~by a staff of Mt. Gongga Station) to compensate for the missing~~ AWS data between July and September 2017 due to equipment inspection and between 29 September and 15 October 2018 due to electrical power failures ~~during this period.~~ During the period 1988-2018, the observed mean annual temperature at 3000 m a.s.l. was 4.5 °C. Rain gauges recorded an average annual ~~number average~~ of 314 days with precipitation with and a mean annual amount of 1912 mm ~~precipitation at 3000 m a.s.l.~~, of which 88% ~~amount~~ was concentrated in the ablation seasons (April to October) and ~42% was concentrated 380 in summer ~~months~~ (July to September).~~

4 Results

4.1 Retreating, thinning and deceleration of the Hailuoguo Glacier

Glacier outlines in 2002, 2016 and 20~~2019~~ (Fig. 1c) were manually delineated based on high resolution images (Google Earth SPOT-5 imagery for 2002, ~~and~~ UAV images for 2016, and ~~PL imagery for 202019~~). Comparison of these outlines shows that 385 the glacier tongue area has reduced from 2.30 ± 0.06 km² to 1.952 ± 0.02 km² (average 0.098 ± 0.03 km² a⁻¹) between 2016 and 20~~2019~~ compared with the period 2002-2016, when it reduced from 2.65 ± 0.01 km² to 2.30 ± 0.06 km² (average 0.03 ± 0.01 km² a⁻¹). Between 2002 and 2016, the position of the glacier terminus showed a moderate retreat (6 ± 0.44 m a⁻¹); whereas during the following ~~four~~three years (2016-20~~2019~~), the terminus retreated more than $220 \pm 50 \pm 1.56$ m ($\sim 542 \pm 0.39$ m a⁻¹). Field observations indicate that the current glacier terminus area was no longer covered by a thicker debris ~~cover~~ as previous status, 390 and frequent collapse along the subglacial outlet channel became the major backwasting process causing the accelerated terminus retreat.

The lower part of the HLG tongue also showed continuous narrowing as it retreats due to ice thinning. Ice surface elevation and velocity along five profile lines (Fig. 3) show that the ice tongue has experienced substantial ice loss and slowdown over 395 the past decades. The longitudinal line (A-A') along the glacial flow direction runs through the entire ablation zone. Between

1966 and 2000, we observed negligible to small changes in the surface elevation of the upper ice tongue ($-0.5\sim 0$ m a⁻¹, between 3400 to 3700 m a.s.l), with a mean lowering the rate of -0.11 m a⁻¹. However, the ice tongue below 3200 m a.s.l (3~4.5 km to the base of the icefall) thinned remarkably as the highest lowering rate up to -2.2 m a⁻¹ near the glacier terminus. In contrast, the thinning rate of the upper ice tongue has greatly increased between 2000 and 2016, with the surface elevation change rate remaining at around -2.0 m a⁻¹. On the other hand, the lower part of the ice tongue (below 3400m) shows a decreasing thinning rate towards the terminus. For transverse profiles B-B' and C-C', rates of surface elevation lowering were much higher during 2000-2016 (-1.8 m a⁻¹) than 1966-2000 ($-0.3\sim 0$ m a⁻¹). In contrast, profiles D-D' and E-E' showed less surface lowering over the past 50 years, with thinning rates remaining around -0.6 m a⁻¹ and -0.9 m a⁻¹, respectively.

Analysis of ice surface velocities during three periods (1982-1983, 2007-2011, and 2014-2018) in the past 38 years (Fig. 3c) indicates that the lower ablation area of HLG has experienced a gradual slowdown, with the rate of this deceleration decreasing of up glacier (Fig. 3c, profile A-A') and with increasing proximity to the lateral margins (Fig. 3c, profiles B-E). Ice surface velocities along all transverse cross sections haves gradually decreased, with the greatest deceleration occurring along with profiles B-B' to D-D' (mean rate of 0.26 m a⁻¹) and less along the E-E' section (mean rate of 0.06 m a⁻¹). Note that remarkable decelerations that happened across the whole transverse profile of D-D' during our observation periods have led the ice tongue below almost stagnated (with a velocity less than 0.1 m a⁻¹) during 2014-2018.

4.2 Paraglacial slope failures

Mapped extents of the ~~paraglacial collapsed areas~~ PBGAs between 1990 and 2020 were presented in Fig. 4. The ~~extents of~~ PEBGA shows continual expansion during the observation period, increased from 0.31 ± 0.27 km² in 1990 to 1.38 ± 0.06 km² in 2020, with a total areal increase of 1.07 ± 0.32 km². Its decadal expansion rates increased from ~ 0.01 km² a⁻¹ in 1990-2000 and 0.02 km² a⁻¹ in 2000-2011, to ~ 0.08 km² a⁻¹ in 2011-2020, which was approximately proportionate to the annual decrease in the GCA. Due to a transient rock-fall below the icefall occurred between September and November 2018, the PBGA area increased significantly, with an expansion rate up to ~ 0.11 km² a⁻¹ (10.43%) from 2018-2019 within one year. In general, the north-facing slope (located on the true right side of the glacier) exhibits more stability than south-facing slope, where 56% of the total PBGA was mapped and lower frequency of PSFs.

~~According to the classification method in Tab. S1. By combining visual analysis of our time series remote sensing and UAV imagery with knowledge of slope material composition, erosion type, and event magnitude, w~~We identified three typical styles of paraglacial slope failure within the PBGA, with a total area of 0.75 ± 0.03 km² in 2020, according to the classification method in Tab. S1 that broadly with classifications proposed by Ballantyne (2002) and McColl (2012) (Fig. 5a):

A. Rock-fall, $0.22\pm 0.06\pm 0.01$ km² in 2020, $8\pm 2\%$ of the total PSF area.

B. ~~S~~sediment-mantled slopes slide, 0.37 ± 0.01 km² in 2020, 49% of the total PSF area. ~~and collapse~~

430 C. ~~G~~ully headward erosion, 0.32 ± 0.01 km² in 2020, 43% of the total PSF area.

Based on calculated surface slope map from the 2016 DEM (Fig. S5) as well as field verifications (Fig. S6), the Type B and C PSFs (with a mean surface slope of 29° and 32°, respectively) usually show lower slopes in their unstable areas than stable areas (40-60°). Mean slope of the Type A PSF is about 54°, which is within the range of the stable slope.

435

Below ~~We will~~ present a detailed ~~case study~~ descriptive analysis ~~of for~~ each type of PSF observed at HLG ~~below~~, and provide a summary of the dimensions and typology ~~of for each~~ specific PSFs identified in Fig. 5a in Table 2.

4.2.1 Rock-falls (~~paraglacial slope failure~~ PSF type A)

Different magnitude rock-falls are common at exposed steep bedrock terrain on both sides of HLG. ~~Evidence of a~~ recent
440 ~~large single~~ rock-fall event (Type A, Fig. 5b) ~~was~~ occurred around October 15, 2018 ~~originating from a~~ south-west facing
~~paraglacial slope high-hanging above the upper HLG ice tongue (4000 m a.s.l., ~450 m high from the glacier surface) at a~~
~~distance of ~0.3 km from the base of the icefall (Fig. 5b). The rockfall deposit and the existing glacier debris cover are slightly~~
~~different in colour and grain size and can thus be clearly delineated on the glacier surface, both on field photograph and on~~
~~remote sensing imagery (Fig. 5b and Fig. S7). The ~~The~~ rock fall final deposition area of the rockfall covers a projected area of~~
445 ~~~47,000 m² is 283 m in width, 200 m in length, 450 m in height from the glacier surface, stretch in~~ covers a vertical height of
380 m, ~~and~~ slope length of 472 m, ~~and a 2D area of ~47,000 m². The (runout length was approximately ~365 m) and the drop~~
~~height 40 m. Based on the extent of the main detachment zone, the deposition thickness (3-5 m estimated during the field visit)~~
~~and area (Fig. 5b), total release volume of the rockfall is 1,000-10,000 m³. The deposit corresponds to an estimated release~~
~~volume of 60,000-100,000 m³ of light green granodiorite rock detached from ~4000 m a.s.l. on a steep south~~ north-facing slope
450 (Fig. 5b). The thickness of the deposit was estimated during a field visit to be 3-5 m and the volumetric estimate is based on
~~the extent of the main detachment zone, and the deposit thickness and area (Fig. 5b). The failed rock block amalgamated~~
~~additional material from below the main detachment zone and ran out on to the surface of HLG, resting supraglacially at~~
~~around 3580 m a.s.l., demonstrating that is possible for sizeable volumes of rock fall to be delivered directly to the supraglacial~~
~~environment in the glacier ablation zone, where it can contribute to debris layer thickening. The rock fall deposit and the~~
455 ~~existing glacier debris cover are slightly different in colour and grain size and can thus be some clearly delineated on the glacier~~
~~surface, both in the field, and on remote sensing imagery (Fig. 5b).~~

We also observed ~~other several suspected~~ major rock-fall scars on the lower part of the valley wall in close proximity to this
scar deposit (i.e., up to 260-400 m above the glacier surface; Fig. 5b and 5c) suggesting that numerous ~~similar smaller~~ scale
460 rock-falls have occurred in this locality. Since the rock surface has been partially weathered and most of the bedrock has been

covered by vegetation such as mosses and shrubs, we speculate that these rock-falls may have occurred earlier and ~~are~~ have not been documented by remote sensing images or literature.

465 ~~Except the 2018 large rockfall. However, the vertical joints of exposed bedrock on both sides of the glacier are well developed, and small magnitude rock falls occur more frequently (Fig. 5a, Fig. S73). Based on UAV images and field investigation, we found identified at least 15 fresh small-magnitude rock-falls in view of their evident talus depositions based on UAV images and field investigation (Fig. 5a, Fig. S7). These small-scale rockfalls are found located on both sides of the lower paraglacial slopes and events have a source area ranging from 59 to 3028 m² on the paraglacial slopes, each with a mean area of 750 m².~~
470 ~~Their disintegrating rock masses were located between 3100 and 3500 m a.s.l. with the a mean vertical distance between from the base and glacier surface is are of about 110 m from their lowest breakpoints to the glacier surface. But, unfortunately, because of due to their small sizes and without continuous observations (e.g., time-lapse photography), we cannot determine the exactly exact time when they happened. These collapsed rock falls falling on the glacier surface of with different magnitude have obviously become are one of the important main ways inputs for supraglacial debris delivery to the glacier surface in the~~
475 ~~lower part of the HLG ice tongue.~~

4.2.2 Sediment-mantled slopes slide and collapse (**paraglacial slope failure PSF type B**)

We identified evidence of four major sediment-mantled slope slides and collapse (Type B, B1-B4, Fig. 5a). Combined, these features cover an area of ~370,000 m² (2019-PL) and are located on both north- and south-facing valley sides. The 2D area of Type B PSFs steadily expanded ~~through four processes: glacier downwasting exposing more of the slope, lateral expansion of~~
480 ~~the failure mass, and headward expansion from retrogressive failure or degradation of the scarp,~~ over our monitoring period (Fig. 4), ~~The with a total area increased by of 297,000 m² from 1990 to 2020, and the an areal expansion rate was of 10.16% a~~
~~1 from 1990 to 2020.~~

485 B1 (3500 m a.s.l, Fig. S26a) is located on a north-facing lateral moraine slope at a distance of 1.5 km from the base of the icefall, and is 114 m wide, 1035 m long, and 112,424 m² in area. Between 2017 and 2019 the exposed area of this feature B1 slope increased by 12,125 m², or a percentage increase of 12.09 %. A landslide with an area of 53,000 m² is included as a nested feature within B1 (48.28% of B1 area), and evidence of superimposed gullying is also found on the eastern, western, and northern segments of this feature. ~~According to the conceptual model designed by Eichel et al. (2018), there are three~~
490 ~~stages which describe the transition from active to stable sediment mantled slopes: (a) gullying, (b) solifluction, (c) stabilization. The B1 feature is typical of stage A, and is characterized by active gullying and evidence of debris flows, slope-wash, slope slides, combining to produce a complex slope landform which hosts pioneer vegetation species and is very geomorphologically active.~~ The UAV images in 2016 did not cover the B1 area completely, so we extracted 23 common tie

points across UAV images from 2017 to 2019 to manually quantify the surface displacement rate; the slope showed downslope
495 displacement of $1.96 \pm 0.04 \text{ cm d}^{-1}$, and a maximum of $2.08 \pm 0.04 \text{ cm d}^{-1}$ in the period 2017-2018.

Feature B2 (3150 m a.s.l, Fig. [S26b](#)) is the largest type B PSF and is located on the true left, south-facing moraine slope close
to the glacier terminus (3240-3120 m a.s.l.). It is fan-shaped with a width of $\sim 262 \text{ m}$, a length of 644 m , a height of $\sim 120 \text{ m}$,
and a total area of $122,738 \text{ m}^2$. In contrast to B1, this feature is characterized as a single landslide without any nested features
500 (e.g., gullies). [Visual a](#)Analysis of satellite imagery shows that detectable slope movement began around the year 2000,
which is consistent with the onset of accelerated lowering of the glacier surface in this region and accompanying debuitressing
of ice-marginal topography. We selected 33 tie points evenly distributed in the B2 landslide area on the four-year UAV images
(2016-2019) to monitor its surface displacement, which revealed that the landslide has [movedfallen](#) by an average of 2.63 ± 0.04
m a^{-1} in the UAV monitoring period, and the affected area has increased by $7,414 \text{ m}^2$ via headscarp erosion. The highest rate
505 of displacement was 4.32 cm d^{-1} and occurred between 2017-2018. Between 2011 and 2019, the collapsed area of B2 has
expanded by $35,000 \text{ m}^2$, with an expansion rate of $4.99\% \text{ a}^{-1}$. The landslide has a vertical glide distance of 48 m , and a horizontal
displacement of 70 m . In the period 2017-2018 landslide activity forced [the](#) closure of a zigzag trail path (Fig. 5e) which was
used for accessing the glacier.

510 Across the valley from B2, we identify landslide B3 (3100 m a.s.l, Fig. 5f, Fig. [S26c](#)), which is 805 m in length, 132 m in width,
and $63,241 \text{ m}^2$ in area and, like B2, is located on a lateral moraine close to the glacier terminus. The landslide has been
effectively divided into five zones, delineated by four gullies (Fig. 5f). Analysis of satellite imagery shows [s](#) that the landslide
began to develop around 2013, when a headscarp is first detectable. Feature tracking (33 tie points) analysis on repeat UAV
images shows that the landslide has moved down with an average rate of $1.65 \pm 0.04 \text{ cm d}^{-1}$ between 2016 and 2019, with the
515 highest rate of $1.97 \pm 0.04 \text{ cm d}^{-1}$ occurring in the period 2017-2018.

Feature B4 (Fig. [S26d](#)) is also located on the north-facing (true right) lateral moraine slope of the glacier, approximately 3.5
km from the base of the icefall. It is $\sim 103 \text{ m}$ in height, 993 m in length, and covers an area of $73,270 \text{ m}^2$. Geomorphologically,
this feature is the most complex of the type B PSFs, in that it represents a transition [slopeform](#) that it exhibits [landslidcsing](#)
520 [behavior](#) in two distinct zones at either end (covering an area of $18,244 \text{ m}^2$, or 24.90% of the sediment-mantled moraine slope
in this area) and also exhibits gully headward erosion (i.e., PSF Type C). Feature tracking analysis of 37 tie points indicates
that the landslide moved downslope at an average rate of $1.66 \pm 0.04 \text{ cm d}^{-1}$ between 2016 and 2019, with a maximum rate of
 $2.63 \pm 0.04 \text{ cm d}^{-1}$ in 2017-2018.

525 4.2.3 Gully headward erosion (~~paraglacial slope failure~~PSF type C)

The three major paraglacial gully headward erosion areas (C1-C3, Fig. 5a) are located at the intersections between three tributary streams which are fed by seasonally snowmelt and the main trunk of the HLG ice tongue. They have a total area of ~324,000 m² in 2019. The UAV images did not cover the entire areas of Type C slopes, therefore we used five-~~PL~~PlanetScope, RapidEye, and Google Earth images from 2002, 2011-2019 to supplement these data and monitor the development of these features (Fig. S87). Our mapping results show that the total area of these three gullies has expanded by ~93,000 m² between 2011 and 2019, with an annual expansion rate of 5.02% a⁻¹.

C1 is located on the northern slope of HLG at an altitude of 3200 m (Fig. 5g; Fig. S87a). In 2019 it had a length of 849 m, a width of 312 m and an area of 139,135 m². It is adjacent to a major tributary stream that drains the northern side of the valley, and which intersects (and bisects) the true left lateral moraine where the glacier turns to flow eastward to its terminus. Field inspection of exposed surfaces at C1 reveals that it comprises a block of thick debris and sand deposits with some finer material, which was previously colonized by vegetation before being denuded by flowing water. In the period 2011-2015, the area of the gully expanded upslope at a rate of 10.44 m a⁻¹, and by 2019 the location of headward erosion was more clearly concentrated in the meltwater tributary channel (Fig. S87a). Between 2011 and 2019, the average upward denudation rate of the feature was 3.39 cm d⁻¹ (12.20 m a⁻¹) and the exposed area had increased by 45,449 m², or 48.59% from 2011 (Tab. 2).

Gully C2 is situated on the southern slope (true right lateral moraine) of HLG at about 3200 m a.s.l (Fig. 5h; Fig. S87b) and in 2019 extended ~160 m in width, ~270 m in length, and 24,248 m² in area. The exposed area of the gully expanded upslope along the path of a meltwater-fed tributary stream, with a gradient of ~36° close to the HLG moraine, and which originates from Hailuoguo No. 3 Glacier (29° 32.41' N, 101° 58.05' E). This tributary stream connects directly to the subglacial water system of HLG. The gully is most actively eroding upstream of the point at which it connects to HLG, with an average upward denudation rate of 0.76 cm d⁻¹ between 2002 and 2019, producing an increase in the exposed-sediment-covered area of 11,923 m² in the same period.

Gully C3 is also located on the southern slope of HLG at 3500 m a.s.l (Fig. 5i; Fig. S87c), around ~800 m west of gully C2. The gully is formed by a tributary stream which is fed by meltwater from Hailuoguo No. 2 Glacier (29° 32.82' N, 101° 56.92' E), which became detached from HLG sometime after the 1930s (Liu and Zhang, 2017) and has since retreated to the edge of an-ice scarp ridge. The gully is filled with glaciofluvially-transported glacial sediment and is deeply incised. Like C2, meltwater also flows into HLG glacier subglacially. Since 2002, expansion of the sediment-mantled area of this gully has occurred on the right (east) side of the gully and has recently begun to expand up along the left (west) bank of the channel. We expand the area of the gully to incorporate adjacent unvegetated lateral moraine, which also shows evidence of gullying and

headward erosion. The total area of C3 increased by 14.3%, from 109,500 m² in 2002 to 160,474 m² in 2019, with an average upward denudation rate of 1.15 cm d⁻¹ between 2002 and 2019.

5 Discussion

560 5.1 Possible forcing mechanism of the three different types of paraglacial slope failures PSFs in at Hailuoguo glacier HLG

Many potential factors, including glacial history (notably mostly downwasting and debuitressing in HLG since Little Ice Age), rock structure (e.g. i.e., joint distribution), seismicity, and short- and long-term local meteorological disturbances (i.e., precipitation, temperature, and freeze-thaw cycling), have been generally considered as preconditioning, preparatory or
565 triggering factors that combine to produce a PSF (McColl, 2012). In the subsections discussion below we refer to these factors to discuss their relative importance in forcing the different types of PSF that we observed at the Hailuoguo HLG glacier.

5.1.1 Rock-fall

Small-scale rockfalls are commonly found sourced from exposed bedrock walls on both sides of the HLG ice tongue. These exposed bedrock walls are generally granite rocks characterised by well-developed vertical joints (Fig. S6 and S7), which
570 make the slope more prone to failure or more likely failure under given triggers (Draebing and Krautblatter, 2019). In addition to slope glacier erosional oversteepening as a result of glacial erosion (Herman et al., 2021), the 'fresh' exposure of these bedrock slopes as a result of glacier thinning can also accelerate the weathering processes and result in a reduction in rock strength degradation (Matsuoka, 2008). Intensification of freeze-thaw conditions during deglaciation may have led to more enhanced rockfall activity since the winter seasons in the at HLG environment is cold enough to cause frozen water to freeze
575 within rock fractures and pore spaces. During Conversely, the warmth and humidity of the summer monsoon seasons, the warm humid environment can also enhance rates of be a stimulative factor leading intense and rapid chemical weathering of the exposed rock walls (Li et al., 2019), and a reduction in rock strength. However, we cannot determine the frequency and magnitude dynamics of these small-scale rockfalls are difficult to be determined by this study in this study because Since it is difficult to determine their specific occurring specific time of their occurrence was unknown and we likely observe a degree
580 of small-scale event censoring many formal rockfalls may be as smaller rockfall scars progressively enlarge via detachment of subsequent rockfall overlapped by later ones during our investigation period. We therefore In the following part of of small rock falls occurred (as mentioned in subsection 4.2.1 above), this section we will focuses on discussing the discussion of possible forcing mechanisms of the discuss the impact factors of the a larger-scale rock fall rockfall event which occurred in 2018, which we could confirm its occurring time (around 15 Oct. 2018) and estimate its magnitude from UAV surveys.

585 The 2018 rock fall rockfall (Fig. 5b) represents a rapid non-ice contact rock collapse adjacent to an area of the glacier that which has experienced remarkable (80-100 m) thinning since its Little Ice Age (LIA) maximum (Fig. 5c). More widely in the

590 Mt. Gongga region, glacial and paraglacial landform assemblages display a strong influence of Late Pleistocene and Holocene
glaciations, the most striking example of which are the deeply incised trunk and tributary valleys formed by higher rates of
glacier erosion (Liu et al., 2009), glaciofluvial activity, and monsoonal precipitation; as such, paraglacial slopes are strongly
modified by local glacial history, making this an important preconditioning and preparatory factor for ~~rock fall~~rockfall.
Anecdotally, small-scale rock collapses occur all year round on both sides of HLG (Fig. 5a; Fig. S73), especially from those
rock slopes exhibiting vertical jointing. Our field investigations indicate that the main detachment zone of the 2018 ~~rock~~
fall~~rockfall~~ has no faults but is highly jointed, which facilitates liquid water ingress and hydraulic erosion and is also conducive
595 to promoting fracturing via freeze-thaw and ice segregation processes (Rodríguez-Rodríguez et al., 2018) which gradually
loosens the rock block and might also be considered a trigger in causing blocks to eventually break away from the rock valley
walls (Fischer et al., 2010).

~~Precipitation and temperature observations near the glacier were analysed to better understand the role of key meteorological
600 factors in causing the large rock fall in 2018.~~ The annual mean temperature was relatively low in 2018 (4.5°C) compared to
the preceding ~~four~~three years (5.0°C, Fig. 6a9). ~~Fig. 6bTab-3 shows the antecedent rainfall in the five to ten days before the
rock fall/rockfall occurred (5-20 Oct 2018) and compares antecedent rainfall statistics between five years (2014-2018). number
of days from 2014 to 2018 with different daily precipitation totals. The mean daily precipitation between 5 and 20 Oct 2018
is 5.89 mm which is significantly higher than 2014, 2015, and 2017, although not significant compared with 2016, the value
605 is still high. We find that 2018 shows a slight precipitation intensity anomaly; the number of days with precipitation totals <
60 mm d⁻¹ is broadly similar to the preceding four years, however, the daily maximum (61mm, 30 June 2018) exceeded that
of the previous four years. A prolonged monsoon, which lasted to the middle of October, was also observed in 2018, and only
one day without precipitation was recorded in the 25 days between 14 September and 09 October (mean daily precipitation of
7.5mm) during which the rock fall occurred.~~ Additionally, ~~the D~~ differences in the daily mean temperature between September
610 to October 2018 and September to October 2014-2017 were relatively large (Fig. 6cS4; ~~from September to October 2018, a
large amount of daily temperature data was missing from the automatic observation and was therefore offset by manual
observations (MO), as mentioned in Section 3.4 above~~); the daily mean temperature was between 0.4 to 5.3°C from 01 to 09
October 2018 compared to a range of 3.6-12.92°C for the preceding four years. From 20 to 29 September, the mean daily
temperature ~~(the observation on 30 September is missing)~~ was similar to the preceding four years with a range of 6.6-13.3°C.
615 The temperature lapse rate (0.0065°C m⁻¹ in humid air, (Hemond and Fechner, 2015)) have shown that when the temperature
at the Gongga Mt. Station (3000 m a.s.l.) drops to about 6°C, the temperature on the mountain at 4000 m a.s.l. approaches 0°C
and ~~begins to~~freezing of water begins. We, therefore, speculate that the abundant precipitation in the early days caused a
large amount of liquid water to ingress the rock fissure, then the frost heave caused the rock mass to eventually rupture (e.g.
(Hartmeyer et al., 2020)). We finally suggest that abnormal precipitation and low temperature in 2018 may have acted as a
620 preparatory factor and triggering factor for the observed ~~rock fall~~rockfall, respectively.

~~Rock fall~~Rockfall and other mass movements can be triggered by seismic activity, which can also act as a preparatory factor through its ability to cause rock damage (Huggel et al., 2007). The HLG region is seismically active, and in the last five years has recorded 9 seismic events ranging from 2.9-3.8 in magnitude, all of which occurred in the period 2016-2017 (China Earthquake Administration, <https://www.cea.gov.cn/>). Although no significant seismic events were observed immediately prior to the 2018 ~~rock fall~~rockfall, rock mass damage associated with the historical seismic activity may have acted as a preparatory factor for the 2018 ~~rock fall~~rockfall and other mass movements from deglaciated slopes in the wider catchment.

5.1.2 Sediment-mantled slopes ~~slide and collapse~~

Type B PSFs are largely associated with lateral moraine instability and collapse. Elsewhere (north-facing slopes, Fig. S9) in the catchment we observe glacially smoothed and polished bedrock surfaces with steep inclination angles (a product of the geological, glacial, and climatic history of the catchment), and we infer that the failure of these unconsolidated slopes is caused by glacier downwasting and debuttressing (Cody et al., 2020), combined with a material angle of repose which is lower than the inclination of the underlying bedrock surface; sediment-mantled slopes ~~hosting~~ showing evidence of instability typically have a slope angle of $\sim 29.5^\circ$, whilst the inclination of exposed bedrock slopes close to the elevation of the present-day glacier surface is $\sim 45^\circ$. Whilst historically the glacier has essentially ‘propped up’ the lateral moraines, rapid reduction in the elevation of the glacier surface has directly contributed to slope instability, which is increasing in speed, corresponding to findings in van Woerkom et al. (2019).

Debris flow may also be a preparatory factor causing slope instability. A gully developing process was observed within Type B failures (as mentioned in Section 4.2.2 above). Based on 17 years (2002-2019) RS monitoring of the B3 slope (Fig. S10), for example, we found that the surficial debris flow occurred before the hillslope movement. Firstly, some debris flows occurred, forming 3 gullies, and no slide was evident in 2002. Secondly, the debris flow gullies gradually expanded, the number increased to 5, the slope slid slightly, and the slide cracks were starting to form around in 2013. Finally, the debris flow gullies increased to 6 and expanded further (the largest gully is about 130 m wide at its widest point), the slope slide significantly (up to 2 cm d⁻¹ between 2017 and 2018; Fig. S2), and the cracks increased in response to rapid glacier downwasting in 2019, which is different from the discovery of the Fox glacier in New Zealand by Cody et al., (2020).

The regional and local climate, which is characterized by abundant precipitation during the monsoon season, enables rapid succession of vegetation on deglaciated slopes. However, although this vegetation is extensive in its coverage, particularly on slopes immediately above the lateral moraines, it mostly comprises species with a shallow rooting depth ~~that~~which do not have a strong capacity to increase slope stability, especially at larger scales; shrub vegetation growing on the unstable B2 and B3 slopes ~~are~~is relatively young and ~~does~~ not mitigate deep translational failure, whereby unconsolidated sediment slides along the interface between the overlying moraine and steep underlying bedrock. We also observed that the displacement of all type B PSFs reached their maximum rate during the period 2017-2018, and upper parts of the slope failures speed up to the same

655 ~~extent as the lower parts (Fig. S3).~~ which may in part be related to increased air temperature (promoting enhanced glacier downwasting) and precipitation extremes in 2018.

5.1.3 Gully headward erosion

660 Glacier downwasting and meltwater from deglaciating tributary catchments enhance erosion of ice-marginal gullies and contribute to the expansion of actively eroding slopes in these landscapes; headward erosion of sidewall tributary gullies occurs as the local base level (i.e., the HLG glacier surface) falls (Williams and Koppes, 2020; Schiefer and Gilbert, 2007), and this effect is illustrated clearly at PSF C1 (Fig. 5g).

The upstream sediments were transported ~~along the transport~~ and accumulated along the gullies to both sides of the glacier, with a fast erosion rate, for instance, the part with the largest change in ~~area of C1~~ area moved ~~travels~~ about 150 m in both 665 horizontal and vertical directions. Therefore, we argue that surface fluvial erosion and glacier debuitressing simultaneously trigger the instability of the type C slopes (Dusik et al., 2019).

All the three major type C slopes are developed along the tributary streams, in which settings slope slides are usually limited but surface fluvial erosion plays the primary role. There should exist a seasonal plus oref enhanced ~~or uprush~~ headward erosion 670 rates, i.e., during the monsoon rainstorm seasons. However, we still could not track this process due to the lack of higher resolution observations in the current study. Nevertheless, it is suggested that this type of paraglacial adjustment is still in active process based on the currently observed situation at both lateral sides of the HLG Hailuoguo Glacier. As the increase of the exposed area and the erosionable baseline, a period of accelerated sediment/debris flux to the surface or base of the glacier is expected in the following years.

675

5.2 Paraglacial geomorphology process in deglaciating monsoon temperate environments Relationships between climate, glacier evolution, local topography and PSF development

This study Our case study at the HLG has demonstrated that paraglacial slopes in the deglaciating monsoon temperate environments are is characterised by the a range of geomorphological process responses, leading to with multi types, fast responding and high rates of landscape denudation. The combination of rapid glacier downwasting exposing unstable moraine and oversteepened bedrock walls with well-developed vertical jointing, and a climate which is conducive to the presence of both freeze-thaw processes and enhanced rates of chemical weathering due to the warmth and high humidity of the summer monsoon season provide favourable conditions for the development of paraglacial slope failures. The following subsection revisits the overall hypothesis of the study, that the climate of warm-wet synchronization is the primary precondition which driving the paraglacial rock and sediment slope failure (Section 5.2.1), and the glacier dynamic change can explain the (prone to) instability of paraglacial slope (Section 5.2.2); and the other implications of paraglacial geomorphology process (Section 5.2.3), which we discuss below. In Mt. Gongga and most SETP monsoon dominate regions, a climate of warm wet synchronization is the primary precondition driving the physical or hydrothermal dynamics of both glacier and off glacier processes.

5.2.1 Impact of the monsoonal climate conditions

Climatic conditions (e.g., fluctuation of temperature and precipitation) can also directly affect slope stability (McColl, 2012;Coe, 2020). Meteorological observations at the Gongga Mountain Station (Fig.1) show that the regional mean annual temperature has increased by about 1 °C over the past 30 years (Fig. 6d). Diurnal (Fig. 6cS14) and annual (Fig. 6a) (Fig. 6) variation of temperature may affect the slope freeze-thaw process (Fischer et al., 2012;Curry et al., 2006). Abundant rainfall (5.89 mm in Section 5.1.1) in the monsoon area-season leads to saturation of glacier-adjacent slopes, and whilst it is well-established that vegetation cover can provide a stabilising effect on regolith, saturation of vegetated slopes nevertheless results their failure.in the absolute high amount precipitation in Mt. Gongga has further promoted the instability of slopes. Small-scale debris flows in the monsoon season are common, which is also the main reason for the occurrence of nested processes in Type B (Fig. 5f, S8b, and S113). The combination of extreme temperature and precipitation ranges conditions can also trigger slope instability (as mentioned in Ssubsection 5.1.1 above - the relatively low temperature and high precipitation in 2018 may be the cause of rockfall).

5.2.2 Paraglacial slope process interaction with the dynamics of temperate glacier

Despite a slowdown in recent decades (Fig. 3c), the flow velocity of HLG is still higher than most mountain glaciers in Himalaya, Tian Shan, and inner Tibet (Bhushan et al., 2018;Wang et al., 2016;Zhang et al., 2010;Ke et al., 2013). Previous work has quantified the evolution of the glacier's subglacial and englacial hydrology, and revealed a highly efficient

hydrological system that is maintained in both summer and winter months (Liu and Liu, 2010); an abundance of meltwater and subglacial and englacial debris (which we infer because of the debris-covered nature of the glacier, e.g. (Miles et al., 2021)) act as effective “grinding tools” for glacial abrasion. The estimated erosion rate is 2.2-11.4 mm a⁻¹ (Based on the current glacier thickness and flow velocity, a conservative estimate of the glacier bedrock erosion depth is about 1-5 m) which is consistent with other temperate glaciers but higher than the continental glaciers (0.1-1.0 mm a⁻¹)(Liu et al., 2009). A high erosion rate contributes to valley incision and the steepening of valley flanks, which increase in exposed area and angle and therefore likely to become more prone to instability.

Warming-induced downwasting of HLG serves as a preparatory or triggering factor for PSFs. Monsoon-Temperate glaciers, particularly those which are steep, are characterised by higher rates of mass turnover (Oerlemans, 1997), and well-developed en- and sub-glacial drainage systems (Fountain and Walder, 1998) which can in monsoon conditions are generally show more remarkable and lead to a faster dynamic responded to the changes of in air temperature and precipitation compared to than cold glaciers (He et al., 2003; Su and Shi, 2002), characterised by high mass turnover and fast flow rate (Oerlemans, 1997), and developed en- and sub-glacial drainage systems (Fountain and Walder, 1998). glaciers found in colder climates (He et al., 2003; Su and Shi, 2002). Glacier downwasting can trigger the failure of Type B and C PSFs (as mentioned in Ssubsection 5.1.2 and 5.1.3 above). According to Fig. 3 and 4, in profile D-D’, the D’ side (true left of the glacier) has been thinned (with a mean rate of -1.0 m a⁻¹) and slowed (the mean daily velocity changed by -0.27 m d⁻¹) more significantly than that on the D side (true right of the glacier; with a mean rate of 0 m a⁻¹ and the mean daily velocity changed by -0.14 m d⁻¹, respectively) in the latest study period, resulting in the slope failure on D’ side has been faster. Bare. The exposed glacier-adjacent slopes may increase the absorption and emission of long-wave thermal radiation on the surface and; contributing to locally the enhanced ablation and surface lowering melting of glaciers in nearby areas of glacier ice. Profile E-E’ showed uniform thinning in both two periods (Fig. 3b, -1.0 m a⁻¹), and we detected, caused the landslides to on appear on both sides of the glacier. For both profiles B-B’ and C-C’, the thinning rate changed from ~0 m a⁻¹ in 1966-2000 to ~-2 m a⁻¹ in 2000-2016 (Fig. 3b), which may be related to the inner stress adjustment in the glacier as -the loss of ice downglacier results in upstream the ice mass of upstream replenishment the acceleration loss of downstream. Both sides of the profile B-B’ are mainly steep bedrock, with a limited accumulation of lateral moraine materials, such that type A is the dominant PSF. The glacier downwasting is mainly used as a preparatory factor for the slope instability; here. The relationship between climatic change, glacier downwasting, and PSFthe three can be is shown in Fig. 7.

Despite a slowdown in recent decades (Fig. 3c), the flow velocity of HLG is still higher than most mountain glaciers in Himalaya, Tian Shan, and inner Tibet (Bhushan et al., 2018; Wang et al., 2016; Zhang et al., 2010; Ke et al., 2013). Previous work has quantified the evolution of the glacier’s subglacial and englacial hydrology, and revealed a highly efficient hydrological system that is maintained in both summer and winter months (Liu and Liu, 2010); an abundance of meltwater and subglacial and englacial debris (which we infer because of the debris covered nature of the glacier, e.g. (Miles et al., 2021))

act as effective “grinding tools” for glacial abrasion. The estimated erosion rate is $2.2\text{--}11.4\text{ mm a}^{-1}$ (Based on the current glacier thickness and flow velocity, a conservative estimate of the glacier bedrock erosion depth is about 1–5 m) which is consistent with other temperate glaciers but higher than the continental glaciers ($0.1\text{--}1.0\text{ mm a}^{-1}$) (Liu et al., 2009). A high erosion rate contributes to valley incision and the steepening of valley flanks, which increase in exposed area and angle and therefore likely to become more prone to instability.

The intense mass flux due to PSFs, on the other hand, can deliver abundant debris materials to the glacier system. According to Fig 4b, the PBGA was equivalent to ~11% of the GCA in 1990 and increased to ~69% in 2020, thereby representing providing an ample source of sediment that could either be delivered to the supraglacial environment, or, through remobilisation, bypass the glacier itself and be transferred to the proglacial for the glacial environment or beyond. For instance, there are many debris fell onto the glacier surface from rockfalls and debris slide/flow process. We calculated (The total areal of all observed rockfalls covered 62216 m^2 (volume class: $10^4\text{--}10^5\text{ m}^3$), which is 2.3% of supraglacial debris-cover area (which is 2.71 km^2 , according to Scherler et al., (2018)) of HLG. ; according to Scherler et al., (2018) the supraglacial debris cover of HLG is 2.71 km^2 , as a result, the total areal contributions to supraglacial debris cover of the rockfalls is 2.3%. Due to the high supraglacial debris-cover of HLG (11-%), the contribution rate of rockfalls observed in this study is lower than that of European Alps and Southern Alps of New Zealand rockfalls of the same size class (Fischer et al., 2012). We also observed a limited number of materials that are delivered to the supraglacial environment through direct roll (Fig. S118 (a); the sediments are more dispersed compared to rockfalls), collapse (Fig. S118 (b)), and debris flow (Fig. S118 (c); faster changes). Among them, two collapsed parts of the B2 slope were quantified by using UAV imagery in the 718 days from 2016/8/31 to 2018/8/19, the collapsed area increased by 94% in total, with an increased rate of $8\text{ m}^2\text{ d}^{-1}$. These sediment delivery process increasing the range and thickness of the supraglacial debris-cover, which in turn affected the surface energy balance for melting and therefore downwasting rate of the glacier, and which will in turn thus influence the rate of runoff meltwater generation production and its contribution to the sea level rise from glacierised catchments. Additionally, some processes (e.g., Type C slope failure) can also deliver materials directly to the sub-glacial environment through via runoff (Fig. S118 (d)). Their contribution to glacial sediments is hard to quantify, but it is clear that this process does result in a long-term and steady sediments supply to the glacier.

Because ice has a lower density than rock (generally 1:3), glacier-adjacent slope instabilities can cause deformation of glacier ice. Finally, failing rock debris may sink into the glacier if the stress they exert exceeds the resistance provided by the glacier ice since rock is higher in density than ice. This geomorphological phenomenon has been identified in the Southern Alps of New Zealand (McColl and Davies, 2013), where mountain glaciers occupy equally steep valleys which bear similarities in steepness and width to our study catchment. Field evidence from the monitoring of the B2 slope by UAV images for four consecutive years (Fig S6b) indicates that the glacier in this vicinity has narrowed or squeezed. The direction of the glacier movement at the boundary with B2 changes as slope B2 advances, which causes the original arc of the glacier boundary to

~~migrato to be destroyed.~~ The greatest change in the location of the glacier boundary bordering slope B2 is during the period 2017-2018, which is consistent with the fastest displacement speed ($\sim 4.32 \text{ cm d}^{-1}$) of the slope during the wider monitoring campaign. Our results may imply that the weight of the moraine may be sufficient to deform the glacier ice, as hypothesized by McColl and Davies (2013).

5.2.3 Other geomorphological and environmental implications

Similar to other studies (Dunning et al., 2015;Glueer et al., 2020;Hedding et al., 2020), our analyses show a temporal and spatial component to PSF development following rapid deglaciation of the HLG. Following many thousands of annual thermo-hydrmechanical loading cycles, which promote rock damage (Grämiger et al., 2017;Glueer et al., 2020) the bedrock slopes bordering HLG are well-prepared for failure, and this response is beginning to manifest as specific triggering events occur and/or mechanical rock mass thresholds are crossed. Similarly, unconsolidated lateral moraines show signs of increasing deformation and translational movement in response to glacier downwasting and debuttressing; we hypothesize that this will continue until critical angles of repose are reached, which will be followed by vegetation colonization and soil development (Eichel et al., 2018).

In respect to the terrain aspect, we found that (He et al., 2003;Su and Shi, 2002;Oerlemans, 1997;Fountain and Walder, 1998)Meteorological observations at nearby Gongga Mountain Station (Fig.1) show that the regional mean annual temperature has increased by about 1°C (Fig. 69) over the past 30 years. Accelerating downwasting of HLG in response to climatic warming serves as a preparatory or triggering factor for PSFs. Through the influence of temperature and precipitation, climatic factors can directly affect slope (in)stability (McColl, 2012;Coe, 2020). Diurnal (Fig. S11) and annual (Fig. 6) variation of temperature may affect the slope freeze-thaw process (Fischer et al., 2012;Curry et al., 2006). Abundant rainfall in the monsoon area results in the absolute high amount precipitation in Mt. Gongga has further promoted the instability of slopes. Small-scale debris flows are common, which is also the main reason for the occurrence of nested processes in Type B (Fig. 5f, S8b, and S13). The combination of extreme temperature and precipitation conditions can also trigger slope instability (as mentioned in subsection 5.1.1 above – the relatively low temperature and high precipitation in 2018 may be the cause of rock fall). On the other hand, climatic factors it can indirectly affect the slope by promoting rock damage over repeated cycles of glacial advance and retreat (Grämiger et al., 2017), and, during periods of sustained negative mass balance (characterized by glacier downwasting and terminus retreat) through slope debuttressing and the failure of consolidated and unconsolidated slopes.

~~Glacier downwasting can trigger the failure of Type B and C (as mentioned in subsection 5.1.2 and 5.1.3 above). According to Fig. 3 and 4, in profile D-D', the D' side has been thinned (with a mean rate of 1.0 m a^{-1}) and slowed (the mean daily velocity changed by -0.27 m d^{-1}) more significantly than that on the D side (with a mean rate of 0 m a^{-1} and the mean daily velocity changed by -0.14 m d^{-1} , respectively) in the latest study period, resulting in the slope failure on~~

D' side has been faster. The exposed slopes may increase the absorption of long-wave thermal radiation on the surface, contributing to the melting of glaciers in nearby areas. Profile E-E' showed uniform thinning in both two periods (Fig. 3b, 1.0 m a^{-1}), caused the landslides to appear on both sides. For both profiles B-B' and C-C', the thinning rate changed from 0 m a^{-1} in 1966-2000 to 2 m a^{-1} in 2000-2016 (Fig. 3b), which may be related to the inner stress adjustment in the glacier—the ice mass of upstream replenishment the acceleration loss of downstream. Both sides of the profile B-B' are mainly steep bedrock, with a limited accumulation of lateral moraine materials, such that type A is the dominant PSF. The glacier downwasting is mainly used as a preparatory factor for the slope instability, here. The relationship between the three can be shown in Fig. 7.

5.2.2 Local topography and PSF development

Despite a slowdown in recent decades (Fig. 3c), the flow velocity of HLG Hailuoguo Glacier is still higher than most mountain glaciers in Himalaya, Tian Shan, and inner Tibet (Bhushan et al., 2018; Wang et al., 2016; Zhang et al., 2010; Ke et al., 2013). Previous work has quantified the evolution of the glacier's subglacial and englacial hydrology, and revealed a highly efficient hydrological system that is maintained in both summer and winter months (Liu and Liu, 2010); an abundance of meltwater and subglacial and englacial debris (which we infer because of the debris-covered nature of the glacier, e.g. (Miles et al., 2021)) act as effective “grinding tools” for glacial abrasion. The estimated erosion rate is $2.2-11.4 \text{ mm a}^{-1}$ (Based on the current glacier thickness and flow velocity, a conservative estimate of the glacier bedrock erosion depth is about 1-5 m) which is consistent with other temperate glaciers but higher than the continental glaciers ($0.1-1.0 \text{ mm a}^{-1}$) (Liu et al., 2009). A high erosion rate contributes to valley incision and the steepening of valley flanks, which increase in exposed area and angle and therefore likely to become more prone to instability.

South-facing slopes show more evidence of instability, both in terms of magnitude and frequency. Firstly, it may be related to the differences in the availability of material (Fig. S9; i.e. asymmetrical deposition of glacial drift and moraine construction on either side of the valley), with more sediment on the south-facing slopes and slope angles (Fig. S9). Secondly, it may be related to the differences in glacier surface altitude and ice thinning rate, which This is particularly obvious compared to the C-C', D-D' and E-E' profiles. It can be seen from profile D-D' in Fig. 3 a, b that the altitude and thinning rate of the glacier under the south-facing slope are much greater than that on the opposite side (ice thinning rate of difference was 1.5 m a^{-1}), which may be caused by the lower surface temperature due to the topographic shading on the glacier areas under the north-facing slope (Liao et al., 2020). Therefore, PSFs and glaciers downwasting show the same temporal and spatial movement in temporal and spatial. This observed pattern further indicates that there is a direct connection between glacier downwasting and PSFs occurrence. Additionally, the unstable slopes are more likely to occur in areas with lower slopes (all-around 30° , as mentioned in Section 4.2 above) is contrary to the general conclusion of the many landslides study - the steeper the slope, the stronger the shear stress and the lower the factor of safety (McColl, 2015), which may be related to the slope material and the failure process.

Additionally, the unstable slopes are more likely to occur in areas with lower slopes (all-around 30° , as mentioned in Section 4.2 above) is contrary to the general conclusion of the many landslides study - the steeper the slope, the stronger the shear stress and the lower the factor of safety (McColl, 2015), which may be related to the slope material and the

845 **failure process. We suggest a conjectural paraglacial slope evolution and slope sediment delivery model of HLG (Fig. 8) to explain this slope anomaly and to explore the logical relationship between the three types of PSFs.**
5.2.3 The contribution of PSFs to supraglacial and sub-glacial environment

850 According to Fig 4b, the PBGA was equivalent to 11% of the GCA in 1990 and increased to 69% in 2020, providing an ample source of sediment for the glacial environment. For instance, there are At the same time, many a large number of debris
fell onto the glacier surface from rock falls and debris slide/flow process. We calculated the total areal of all observed rock
falls covered 62216 m² (volume class: 10⁴–10⁵ m³); according to Scherler et al., (2018) the supraglacial debris cover of HLG
is 2.71 km², as a result, the total areal contributions to supraglacial debris cover of the rock falls is 2.3%. Due to the high
supraglacial debris cover of HLG (11 %), the contribution rate of rockfalls observed in this study is lower than that of Europe
Alps and Southern Alps of New Zealand rock falls of the same class (Fischer et al., 2012). We also observed a limited number
855 of materials that are delivered to the supraglacial environment through direct roll (Fig. S8 (a); the sediments are more dispersed
compared to rock falls), collapse (Fig. S8 (b)), and debris flow (Fig. S8 (c); faster changes). Among them, two collapsed parts
of the B2 slope were quantified by using UAV imagery in the 718 days from 2016/8/31 to 2018/8/19, the collapsed area
increased by 94% in total, with an increased rate of 8 m² d⁻¹. These sediment delivery process increasing the range and thickness
of the supraglacial debris cover, which in turn affected the surface energy balance for melting and therefore downwasting rate
860 of the glacier, which will thus influence the rate of runoff generation and its contribution to the sea level rise from glacierised
catchments, temperature and downwasting of the glacier and the climate. Additionally, some process (e.g., Type C slopes) can
also deliver materials to sub-glacial environment through runoff (Fig. S8 (d)). Their contribution to glacial sediments is hard
to quantify, but it is clear that this process does result in a long term and steady sediments supply to the glacier.

5.2.4 A conjectural model of paraglacial slope evolution and sediment delivery

865 After the glacier was downwasting from the initial state (Stage I), the upper of the steep moraine slope quickly destabilized,
making the entire slope slow, corresponding to funding in van Woerkom et al. (2019), Ballantyne (2013), and Cully et al.
(2006); then the moraine slope slowly slides down (Stage II; which were observed in Type B and part of Type C). During the
870 exposure of the moraine, vegetation may be colonized, or gullies may be formed by debris (or water) flows washing away
(stage II a); when the gullies gradually expand, headward erosion may occur in the upper of the gullies (Stage II b; which were
observed in Type C). Sediments at the base of the slope or fell onto the glacier surface are transferred again as the glacier
moves (Stage III); until the slope is steepest (>50°) when moraine has been removed and bedrock is completely exposed to the
ground, and may collapse through some disturbances, finally (Stage IV; Type A).

875

5.3 Geomorphological and environmental implications

880 Similar to other studies (Dunning et al., 2015; Glueer et al., 2020; Hedding et al., 2020) our analyses show a temporal and spatial component to PSF development following rapid deglaciation. Following many thousands of annual thermo-hydronechanical loading cycles, which promote rock damage (Grämiger et al., 2017; Glueer et al., 2020) the bedrock slopes bordering HLG are well-prepared for failure, and this response is beginning to manifest as specific triggering events occur and/or mechanical rock mass thresholds are crossed. Similarly, unconsolidated lateral moraines show signs of increasing deformation and translational movement in response to glacier downwasting and debuitressing; we hypothesize that this will continue until critical angles of repose are reached, which will be followed by vegetation colonization and advanced soil development (Eichel et al., 2018).

885 Earlier in this article, we posited that the buttressing effect of ice prevented slope movement, and that slope deformation that we observed were largely a response to debuitressing. In the case of lateral moraine evolution, this is likely to be true. However, it is feasible that, since ice is lower in density than rock, failing *rock* slopes may move *into* the glacier if the stress they exert exceeds the resistance provided by the glacier ice. This geomorphological phenomena has been identified in the Southern Alps of New Zealand (McColl and Davies, 2013), where mountain glaciers occupy equally steep valleys. Field evidence from the monitoring of the B2 slope by UAV images for four consecutive years (Fig S6b) indicates that the glacier in this vicinity has narrowed or squeezed. The direction of the glacier movement at the boundary with B2 changes as B2 advances, which causes the original arc of the glacier boundary to be destroyed. The greatest change in the location of the glacier boundary bordering slope B2 aisre during the period 2017-2018, which is consistent with the fastest displacement speed (-4.32 cm d^{-1}) of the slope during the wider monitoring campaign. Our results may imply that the weight of the moraine may be sufficient to deform the glacier ice, as hypothesized by McColl and Davies (2013).

900 Due to the warm and humid climate of the region, the LIA preglacial zone (2980-2800 m) of Hailuogou Glacier is characterized by a fast primary ecological succession landscape, characterized by succession community from cold-adapted herbaceous to *Abies fabri* forest. Glacier downwasting and permafrost thaw have led to accelerated paraglacial erosion and increased frequency of occurred the proglacial debris flow and flash flood, which has occasionally disturbed the established preglacial vegetation (Lu and Gao, 1992). Accumulated surface moraine debris near the lowest ice tongue has suppressed local ice ablation and promoted ice stagnation, and in some locations, this stagnation has led to the establishment of supraglacial vegetation, although this colonization is typically ephemeral due to ice cliff backwasting, for example.

6 Conclusion

905 We used repeat UAV and satellite remote sensing imagery as the basis for identifying and analysing the evolution of three styles of paraglacial slope failure at HLG Hailouogou Hailuogou Glacier between 1990 and 2020; and explore these results in the context of their potential driving mechanisms. Over this period the glacier terminus has retreated $\sim 4510 \text{ m}$ (175 m a^{-1}), its

910 surface has down-wasted by -0.88 m a^{-1} , with thinning observed over 83.50% of the ablation zone study area, and the glacier velocity has slowed from a mean of 0.32 m d^{-1} (period 1982 to 1983) to 0.11 m d^{-1} (2014 to 2018). Rapid downwasting of the glacier surface has exposed oversteepened ice-marginal slope topography, which shows evidence of the overall paraglacial bare ground area (PBGA) increased from $0.31 \pm 0.27 \text{ km}^2$ in 1990 to $1.38 \pm 0.06 \text{ km}^2$ in 2020; and which show evidence of widespread instability in the form of (A~~i~~) ~~rock fall/rockfall and debris avalanching~~ from bedrock slopes, (B~~ii~~) ~~slide/collapse~~ of unconsolidated lateral moraines, and (C~~iii~~) increased erosion activity in tributary valleys, with a total area of $0.75 \pm 0.03 \text{ km}^2$ in 2020. South-facing valley slopes (true left of the glacier) exhibited more destabilization (56% of the total PSFs area) and higher PSF activity than north-facing (true right) valley slopes (44% of the total PSFs area). Set against a background of frequent, small-scale ~~rock fall/rockfalls~~ that are anecdotally recorded in the area, a large ~~rock fall/rockfall~~ occurred in Autumn 2018. Non-ice-contact ~~rock fall/rockfalls~~ in deglaciating catchments are a well-established, short- to long-term response of paraglacial slopes following glacier downwasting and rock slope exposure, however, analysis of antecedent meteorological conditions suggests that an abundant precipitation ~~abnormally long monsoon~~ and low temperature may have served to prepare, and perhaps trigger this rock slope failure. Deformation of sediment-mantled moraine slopes (mean $1.65\text{-}2.63 \pm 0.04 \text{ cm d}^{-1}$) and an increase in erosion activity in ice-marginal tributary valleys caused by a drop in local base level (gully headward erosion rates are $0.76\text{-}3.39 \text{ cm d}^{-1}$) have occurred in tandem with recent glacier downwasting. The PSFs and even the whole paraglacial bare ground area providing an ample source of sediment for the glacial environment. Base of the analysis of paraglacial slope evolution and slope sediment delivery. ~~We speculated that the occurrence of some unstable slopes in the lower slope angle areas may be related to the slope material and the failure process. These two factors combined with glacier dynamic, local topography and other factors, contribute to spatial heterogeneity of paraglacial geomorphology process. Considering our discussion and initial hypothesis, the high erosion rate of HLG associated with the high flow velocity (0.11 m d^{-1} or 40 m a^{-1}) contributes to valley incision and steepening of valley flanks which increase in exposed areas and therefore likely explain that the slope is more prone to instability after accelerating downwasting of the glacier.~~ ~~Field evidence indicates that the glacier ice body adjacent to unstable rock and sediment-mantled slopes has narrowed, or 'squeezed', and we hypothesize that this may be the result of ice deformation caused by ice-marginal slope displacement and loading, but which requires further field investigation.~~ In general, the formation, evolution, and current status of these typical PSFs are generally related to the history of glacier dynamics and paraglacial geomorphological adjustments, and also influenced and/or disturbed by the fluctuation of air temperature/precipitation and their combinations. Longer-term monitoring will provide a clearer picture of the feedbacks between (accelerating) glacier downwasting, climatic conditions, and paraglacial landscape response in this data-poor region.

Data availability

940 The paraglacial slope failure shape files can be requested by email from the author zhongyan19@mails.ucas.ac.cn

Author contributions

QL and XL initiated the underlying research project and obtained the funding. QL developed the research goal and designed the study. QL, YN, BZ, JC, HL and GL performed the primary UAV data. QL and YZ conducted and analysed the data. YZ, QL, MW, YN and FP wrote the paper.

945 Competing interests

The authors declare that they have no conflict of interest.

Acknowledgements

This work was funded by the NSFC Project (41871069) and the Sichuan Science and Technology Programs (2021JDJQ0009, 2020JDJQ0002). The authors gratefully acknowledge the PlanetLab for provision of PlanetScope and RapidEye imagery, and
950 U.S. Geological Survey for Landsat satellite images. MW and FP acknowledge funding from Royal Society-Newton Fund project ‘Understanding glacier and hydrological changes in the Tibetan Plateau using high-resolution monitoring and modelling’.

References

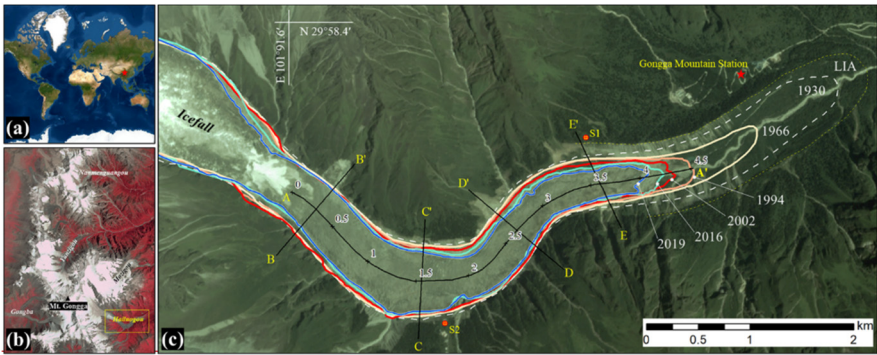
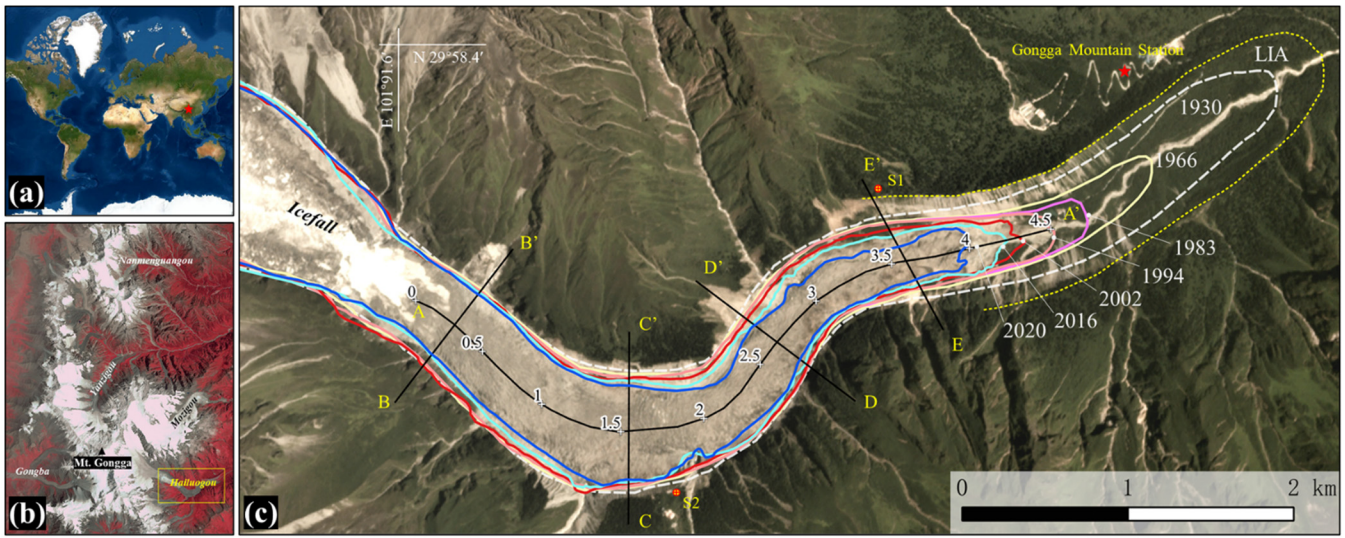
- Ballantyne, C.: Paraglacial landsystems, *Glacial Landsystems*. Arnold, London, 432, 461, 2003.
- 955 Ballantyne, C. K., and Benn, D. I.: Paraglacial Slope Adjustment and Resedimentation following Recent Glacier Retreat, Fåbergstølsdalen, Norway, *Arctic and Alpine Research*, 26, 255-269, doi:10.1080/00040851.1994.12003065, 1994.
- Ballantyne, C. K.: Paraglacial geomorphology, *Quaternary Science Reviews*, 21, 1935-2017, doi:10.1016/S0277-3791(02)00005-7, 2002.
- Ballantyne, C. K.: PERMAFROST AND PERIGLACIAL FEATURES | Paraglacial Geomorphology, in: *Encyclopedia of Quaternary Science (Second Edition)*, edited by: Elias, S. A., and Mock, C. J., Elsevier, Amsterdam, 553-565, 2013.
- 960 Ballantyne, C. K., Wilson, P., Gheorghiu, D., and Rodés, À.: Enhanced rock-slope failure following ice-sheet deglaciation: timing and causes, *earth surface processes and landforms*, 39, 900-913, doi:10.1002/ESP.3495, 2014.
- Bhushan, S., Syed, T. H., Arendt, A. A., Kulkarni, A. V., and Sinha, D.: Assessing controls on mass budget and surface velocity variations of glaciers in Western Himalaya, *Scientific Reports*, 8, 8885, doi:10.1038/s41598-018-27014-y, 2018.
- 965 Boulton, G. S.: Boulder shapes and grain-size distributions of debris as indicators of transport paths through a glacier and till genesis, *Sedimentology*, 25, 773-799, <https://doi.org/10.1111/j.1365-3091.1978.tb00329.x>~~https://doi.org/10.1111/j.1365-3091.1978.tb00329.x~~, 1978.
- Brun, F., Berthier, E., Wagnon, P., Kääb, A., and Treichler, D.: A spatially resolved estimate of High Mountain Asia glacier mass balances from 2000 to 2016, *Nature Geoscience*, 10, 668-673, doi:10.1038/ngeo2999, 2017.
- 970 Cai, J., Jia, H., Liu, G., Zhang, B., Liu, Q., Fu, Y., Wang, X., and Zhang, R.: An Accurate Geocoding Method for GB-SAR

- Images Based on Solution Space Search and Its Application in Landslide Monitoring, *Remote Sensing*, 13, 832, doi:10.3390/rs13050832, 2021.
- Cao, B., Pan, B., Guan, W., Wen, Z., and Wang, J.: Changes in glacier volume on Mt. Gongga, southeastern Tibetan Plateau, based on the analysis of multi-temporal DEMs from 1966 to 2015, *Journal of Glaciology*, 65, 366-375, 2019.
- 975 Chen, C., Zhang, L. M., Xiao, T., and He, J.: Barrier lake bursting and flood routing in the Yarlung Tsangpo Grand Canyon in October 2018, *Journal of Hydrology*, 583, doi:10.1016/j.jhydrol.2020.124603, 2020.
- Cheng, Z. L., Liu, J. J., and Liu, J. K.: Debris flow induced by glacial lake break in southeast Tibet, *Transactions on Engineering Sciences*, 67, 101-111, doi:10.2495/DEB100091, 2010.
- 980 Church, M., and Ryder, J. M.: Paraglacial Sedimentation: A Consideration of Fluvial Processes Conditioned by Glaciation, *GSA Bulletin*, 83, 3059-3072, doi:10.1130/0016-7606(1972)83[3059:psacof]2.0.co;2, 1972.
- Cody, E., Anderson, B. M., McColl, S. T., Fuller, I. C., and Purdie, H. L.: Paraglacial adjustment of sediment slopes during and immediately after glacial debuitressing, *Geomorphology*, 371, 107411, doi:10.1016/j.geomorph.2020.107411, 2020.
- Coe, J. A.: Bellwether sites for evaluating changes in landslide frequency and magnitude in cryospheric mountainous terrain: a call for systematic, long-term observations to decipher the impact of climate change, *Landslides*, 17, 2483-2501, doi:10.1007/s10346-020-01462-y, 2020.
- 985 Cook, S. J., Porter, P. R., and Bendall, C. A.: Geomorphological consequences of a glacier advance across a paraglacial rock avalanche deposit, *Geomorphology*, 189, 109-120, doi:10.1016/j.geomorph.2013.01.022, 2013.
- Curry, A. M., Cleasby, V., and Zukowskyj, P.: Paraglacial response of steep, sediment-mantled slopes to post-'Little Ice Age' glacier recession in the central Swiss Alps, *Journal of Quaternary Science*, 21, 211-225, 10.1002/jqs.954, 2006.
- 990 Deline, P., Gruber, S., Delaloye, R., Fischer, L., Geertsema, M., Giardino, M., Hasler, A., Kirkbride, M., Krautblatter, M., and Magnin, F.: Ice loss and slope stability in high-mountain regions, in: *Snow and Ice-related hazards, risks and disasters*, Elsevier, 521-561, 2015a.
- Deline, P., Hewitt, K., Reznichenko, N., and Shugar, D.: Chapter 9 - Rock Avalanches onto Glaciers, in: *Landslide Hazards, Risks and Disasters*, edited by: Shroder, J. F., and Davies, T., Academic Press, Boston, 263-319, 2015b.
- 995 Draebing, D., and Krautblatter, M.: The Efficacy of Frost Weathering Processes in Alpine Rockwalls, *Geophysical Research Letters*, 46, 6516-6524, doi:10.1029/2019GL081981, 2019.
- Dunning, S. A., Rosser, N. J., McColl, S. T., and Reznichenko, N. V.: Rapid sequestration of rock avalanche deposits within glaciers, *Nat Commun*, 6, 7964, doi:10.1038/ncomms8964, 2015.
- Dusik, J.-M., Neugirg, F., and Haas, F.: Slope Wash, Gully Erosion and Debris Flows on Lateral Moraines in the Upper Kaunertal, Austria, in: *Geomorphology of Proglacial Systems: Landform and Sediment Dynamics in Recently Deglaciated Alpine Landscapes*, edited by: Heckmann, T., and Morche, D., Springer International Publishing, Cham, 177-196, 2019.
- 1000 Eichel, J., Krautblatter, M., Schmidlein, S., and Dikau, R.: Biogeomorphic interactions in the Turtmann glacier forefield, Switzerland, *Geomorphology*, 201, 98-110, doi:10.1016/j.geomorph.2013.06.012, 2013.
- Eichel, J., Draebing, D., and Meyer, N.: From active to stable: Paraglacial transition of Alpine lateral moraine slopes, *Land Degradation & Development*, 29, 4158-4172, 10.1002/ldr.3140, 2018.
- 1005 Emmer, A., Klimeš, J., Hölbling, D., Abad, L., Draebing, D., Skalák, P., Štěpánek, P., and Zahradníček, P.: Distinct types of landslides in moraines associated with the post-LIA glacier thinning: Observations from the Kinzl Glacier, Huascarán, Peru, *Science of The Total Environment*, 739, 139997, doi:10.1016/j.scitotenv.2020.139997, 2020.
- Fan, J., An, C., Zhang, X., Li, X., and Tan, J.: Hazard assessment of glacial lake outburst floods in Southeast Tibet based on RS and GIS technologies, *International Journal of Remote Sensing*, 40, 4955-4979, doi:10.1080/01431161.2019.1577578, 2019.
- 1010 Farr, T. G., Rosen, P. A., Caro, E., Crippen, R., Duren, R., Hensley, S., Kobrick, M., Paller, M., Rodriguez, E., Roth, L., Seal, D., Shaffer, S., Shimada, J., Umland, J., Werner, M., Oskin, M., Burbank, D., and Alsdorf, D.: The Shuttle Radar Topography Mission, *Reviews of Geophysics*, 45, doi:10.1029/2005RG000183, 2007.
- 1015 Fickert, T., and Grüniger, F.: High-speed colonization of bare ground—Permanent plot studies on primary succession of plants in recently deglaciated glacier forelands, *Land Degradation & Development*, 29, 2668-2680, doi:10.1002/ldr.3063, 2018.
- Fischer, L., Amann, F., Moore, J. R., and Huggel, C.: Assessment of periglacial slope stability for the 1988 Tschierwa rock avalanche (Piz Morteratsch, Switzerland), *Engineering Geology*, 116, 32-43, doi:10.1016/j.enggeo.2010.07.005, 2010.
- 1020 Fischer, L., Purves, R. S., Huggel, C., Noetzli, J., and Haerberli, W.: On the influence of topographic, geological and cryospheric factors on rock avalanches and rockfalls in high-mountain areas, *Nat. Hazards Earth Syst. Sci.*, 12, 241-254,

- 10.5194/nhess-12-241-2012, 2012.
- Fountain, A. G., and Walder, J. S.: Water flow through temperate glaciers, *Reviews of Geophysics*, 36, 299-328, 1998.
- 1025 Fyffe, C. L., Woodget, A. S., Kirkbride, M. P., Deline, P., Westoby, M. J., and Brock, B. W.: Processes at the margins of supraglacial debris cover: Quantifying dirty ice ablation and debris redistribution, *Earth Surface Processes and Landforms*, 45, 2272-2290, doi:10.1002/esp.4879, 2020.
- Glueer, F., Loew, S., and Manconi, A.: Paraglacial history and structure of the Moosfluh Landslide (1850–2016), Switzerland, *Geomorphology*, 355, 106677, doi:10.1016/j.geomorph.2019.02.021, 2020.
- 1030 Grämiger, L. M., Moore, J. R., Gischig, V. S., Ivy-Ochs, S., and Loew, S.: Beyond debuitressing: Mechanics of paraglacial rock slope damage during repeat glacial cycles, *Journal of Geophysical Research: Earth Surface*, 122, 1004-1036, doi:10.1002/2016JF003967, 2017.
- Gruber, S., Fleiner, R., Guegan, E., Panday, P., Schmid, M. O., Stumm, D., Wester, P., Zhang, Y., and Zhao, L.: Review article: Inferring permafrost and permafrost thaw in the mountains of the Hindu Kush Himalaya region, *The Cryosphere*, 11, 81-99, 10.5194/tc-11-81-2017, 2017.
- 1035 Haiguanju: Hailuogou Scenic Area achieved another record in tourist reception in 2019, <http://www.gzz.gov.cn/gzzrmzf/c100044/202001/38048f67a8d3431fa8fe98d250b42281.shtml>, 2020.
- Haritashya, U. K., Kargel, J. S., Shugar, D. H., Leonard, G. J., Strattman, K., Watson, C. S., Shean, D., Harrison, S., Mandli, K. T., and Regmi, D.: Evolution and Controls of Large Glacial Lakes in the Nepal Himalaya, remote sensing, 10, doi:10.3390/RS10050798, 2018.
- 1040 Hartmeyer, I., Delleske, R., Keuschmig, M., Krautblatter, M., Lang, A., Schrott, L., and Otto, J. C.: Current glacier recession causes significant rockfall increase: the immediate paraglacial response of deglaciating cirque walls, *Earth Surf. Dynam.*, 8, 729-751, doi:10.5194/esurf-8-729-2020, 2020.
- He, Y., Zhang, Z., H.Theakstone, W., Chen, T., Yao, T., and Pang, H.: Changing features of the climate and glaciers in China's monsoonal temperate glacier region, *Journal of Geophysical Research*, 108, 4530-4536, 2003.
- 1045 He, Y., Li, Z., Yang, X., Jia, W., He, X., Song, B., Zhang, N., and Liu, Q.: Changes of the Hailuogou Glacier, Mt. Gongga, China, against the background of global warming in the last several decades, *Journal of China University of Geosciences*, 19, 271-281, 2008.
- Hedding, D. W., Erofeev, A. A., Hansen, C. D., Khon, A. V., and Abbasov, Z. R.: Geomorphological processes and landforms of glacier forelands in the upper Aktru River basin (Gornyi Altai), Russia: evidence for rapid recent retreat and paraglacial adjustment, *Journal of Mountain Science*, 17, 824-837, doi:10.1007/s11629-019-5845-5, 2020.
- 1050 Hemond, H. F., and Fechner, E. J.: Chapter 4 - The Atmosphere, in: *Chemical Fate and Transport in the Environment (Third Edition)*, edited by: Hemond, H. F., and Fechner, E. J., Academic Press, Boston, 311-454, 2015.
- Hewitt, K., Clague, J., and Deline, P.: Catastrophic Rock Slope Failures and Mountain Glaciers, in: *Encyclopedia of Snow, Ice and Glaciers*, edited by: Singh, V. P., Singh, P., and Haritashya, Springer, pp. 113-126, 2011.
- 1055 Hu, G., Chen, N., Deng, M., and Wang, Y.: Classification and Initiation Conditions of Debris Flows in Linzhi Area, Tibet, *Bulletin of Soil and Water Conservation*, 31, 193-197+221, 2011.
- Huggel, C., Caplan-Auerbach, J., Waythomas, C. F., and Wessels, R. L.: Monitoring and modeling ice-rock avalanches from ice-capped volcanoes: A case study of frequent large avalanches on Iliamna Volcano, Alaska, *Journal of Volcanology and Geothermal Research*, 168, 114-136, doi:10.1016/j.jvolgeores.2007.08.009, 2007.
- 1060 Hungr, O., Leroueil, S., and Picarelli, L.: The Varnes classification of landslide types, an update, *Landslides*, 11, 167-194, doi:10.1007/s10346-013-0436-y, 2014.
- Jarman, D.: Large rock slope failures in the Highlands of Scotland: Characterisation, causes and spatial distribution, *engineering geology*, 83, 161-182, doi:10.1016/J.ENGCEO.2005.06.030, 2006.
- 1065 Kääb, A., Jacquemart, M., Gilbert, A., Leinss, S., Girod, L., Huggel, C., Falaschi, D., Ugalde, F., Petrakov, D., Chernomorets, S., Dokukin, M., Paul, F., Gascoïn, S., Berthier, E., and Kargel, J. S.: Sudden large-volume detachments of low-angle mountain glaciers – more frequent than thought?, *the cryosphere*, 15, 1751-1785, doi:10.5194/TC-15-1751-2021, 2021.
- Ke, C.-Q., Kou, C., Ludwig, R., and Qin, X.: Glacier velocity measurements in the eastern Yigong Zangbo basin, Tibet, China, *journal of glaciology*, 59, 1060-1068, doi:10.3189/2013JOG12J234, 2013.
- Kirkbride, M. P., and Deline, P.: Spatial heterogeneity in the paraglacial response to post-Little Ice Age deglaciation of four headwater cirques in the Western Alps, *Land Degradation & Development*, 29, 3127-3140, doi:10.1002/ldr.2975, 2018.
- 1070 Li, X., Ding, Y., Liu, Q., Zhang, Y., Han, T., Jing, Z., Yu, Z., Li, Q., and Liu, S.: Intense Chemical Weathering at Glacial

- Meltwater-Dominated Hailuogou Basin in the Southeastern Tibetan Plateau, *Water*, 11, 10.3390/w11061209, 2019.
- Li, Z., He, Y., Yang, X., Theakstone, W. H., Jia, W., Pu, T., Liu, Q., He, X., Song, B., Zhang, N., Wang, S., and Du, J.: Changes of the Hailuogou glacier, Mt. Gongga, China, against the background of climate change during the Holocene, *Quaternary International*, 218, 166-175, doi:10.1016/j.quaint.2008.09.005, 2010.
- 1075 Liao, H., Liu, Q., Zhong, Y., and Lu, X.: Landsat-Based Estimation of the Glacier Surface Temperature of Hailuogou Glacier, Southeastern Tibetan Plateau, Between 1990 and 2018, remote sensing, 12, doi:10.3390/RS12132105, 2020.
- Liu, G., Chen, Y., Zhang, Y., and Fu, H.: Mineral deformation and subglacial processes on ice-bedrock interface of Hailuogou Glacier, *Chinese Science Bulletin*, 54, 3318-3325, doi:10.1007/s11434-009-0289-x, 2009.
- 1080 Liu, G., Zhang, B., Liu, Q., Zhang, R., Cai, J., Fu, Y., Yu, B., and Li, Z.: Monitoring Dynamics of Hailuogou Glacier and the Secondary Landslide Disasters Based on Combination of Satellite SAR and Ground-Based SAR, *Geomatics and Information Science of Wuhan University*, 44, 980-995, 2019a.
- Liu, J., Zhang, J., Gao, B., Li, Y., Mengyu, L., Wujin, D., and Zhou, L.: An overview of glacial lake outburst flood in Tibet, China, *Journal of Glaciology and Geocryology*, 41, 1335-1347, 2019b.
- 1085 Liu, Q., and Liu, S.: Seasonal evolution of the englacial and subglacial drainage systems of a temperate glacier revealed by hydrological analysis, *Sci. Cold Arid. Reg.*, 2, 51-58, 2010.
- Liu, Q., Liu, S., Zhang, Y., Wang, X., Zhang, Y., Guo, W., and Xu, J.: Recent shrinkage and hydrological response of Hailuogou glacier, a monsoon temperate glacier on the east slope of Mount Gongga, China, *Journal of Glaciology*, 56, 215-224, 2010.
- Liu, Q., and Zhang, Y.: Studies on the dynamics of monsoonal temperate glaciers in Mt. Gongga: a review, *Mountain Research*, 35, 717-726, 2017.
- 1090 Liu, Q., Liu, S., and Cao, W.: Seasonal Variation of Drainage System in the Lower Ablation Area of a Monsoonal Temperate Debris-Covered Glacier in Mt. Gongga, South-Eastern Tibet, *Water*, 10, 1050, 2018.
- Liu, W., Carling, P. A., Hu, K., Wang, H., Zhou, Z., Zhou, L., Liu, D., Lai, Z., and Zhang, X.: Outburst floods in China: A review, *earth science reviews*, 197, doi:10.1016/J.EARSCIREV.2019.102895, 2019c.
- 1095 Matsuoka, N.: Frost weathering and rockwall erosion in the southeastern Swiss Alps: Long-term (1994–2006) observations, *geomorphology*, 99, 353-368, doi:10.1016/J.GEOMORPH.2007.11.013, 2008.
- McColl, S. T.: Paraglacial rock-slope stability, *Geomorphology*, 153-154, 1-16, doi:10.1016/j.geomorph.2012.02.015, 2012.
- McColl, S. T., and Davies, T. R.: Large ice-contact slope movements: glacial buttressing, deformation and erosion, *Earth Surface Processes and Landforms*, 38, 1102-1115, 2013.
- 1100 McColl, S. T.: Chapter 2 - Landslide Causes and Triggers, in: *Landslide Hazards, Risks and Disasters*, edited by: Shroder, J. F., and Davies, T., Academic Press, Boston, 17-42, 2015.
- Miles, K. E., Hubbard, B., Miles, E. S., Quincey, D. J., Rowan, A. V., Kirkbride, M., and Hornsey, J.: Continuous borehole optical televueing reveals variable englacial debris concentrations at Khumbu Glacier, Nepal, *Communications Earth & Environment*, 2, 12, doi:10.1038/s43247-020-00070-x, 2021.
- 1105 Neckel, N., Loibl, D., and Rankl, M.: Recent slowdown and thinning of debris-covered glaciers in south-eastern Tibet, *Earth and Planetary Science Letters*, 464, 95-102, 10.1016/j.epsl.2017.02.008, 2017.
- Oerlemans, J.: Climate sensitivity of Franz Josef Glacier, New Zealand, as revealed by numerical modeling, *Arctic and Alpine Research*, 29, 233-239, 1997.
- 1110 Pan, B., Zhang, G., Wang, J., Cao, B., Geng, H., Zhang, C., and Ji, Y.: Glacier changes from 1966-2009 in the Gongga Mountains, on the south-eastern margin of the Qinghai-Tibetan Plateau and their climatic forcing, *The Cryosphere*, 6, 1087, 2012.
- Reheis, M. J.: Source, transportation and deposition of debris on Arapaho Glacier, Front Range, Colorado, U.S.A, *journal of glaciology*, 14, 407-420, 10.1017/S0022143000021936, 1975.
- Reznichenko, N. V., Davies, T. R. H., Shulmeister, J., and Larsen, S. H.: A new technique for identifying rock avalanche-sourced sediment in moraines and some paleoclimatic implications, *Geology*, 40, 319-322, doi:10.1130/g32684.1, 2012.
- 1115 Rodríguez-Rodríguez, L., González-Lemos, S., Ballesteros, D., Valenzuela, P., Domínguez-Cuesta, M. J., Llana-Fúnez, S., and Jiménez-Sánchez, M.: Timing of paraglacial rock-slope failures and denudation signatures in the Cantabrian Mountains (North Iberian Peninsula), *Land Degradation & Development*, 29, 3159-3173, doi:10.1002/ldr.3012, 2018.
- 1120 Rowan, A. V., Quincey, D. J., Gibson, M. J., Glasser, N. F., Westoby, M. J., Irvine-Fynn, T. D. L., Porter, P. R., and Hambrey, M. J.: The sustainability of water resources in High Mountain Asia in the context of recent and future glacier change, *Geological Society, London, Special Publications*, 462, 189, doi:10.1144/SP462.12, 2018.

- Salerno, F., Thakuri, S., D'Agata, C., Smiraglia, C., Manfredi, E. C., Viviano, G., and Tartari, G.: Glacial lake distribution in the Mount Everest region: Uncertainty of measurement and conditions of formation, global and planetary change, 92, 30-39, doi:10.1016/J.GLOPLACHA.2012.04.001, 2012.
- 1125 Scherler, D., Wulf, H., and Gorelick, N.: Global Assessment of Supraglacial Debris-Cover Extents, *Geophysical Research Letters*, 45, 11,798-711,805, doi:10.1029/2018GL080158, 2018.
- Schiefer, E., and Gilbert, R.: Reconstructing morphometric change in a proglacial landscape using historical aerial photography and automated DEM generation, *Geomorphology*, 88, 167-178, doi:10.1016/j.geomorph.2006.11.003, 2007.
- 1130 Shugar, D. H., Jacquemart, M., Shean, D., Bhushan, S., Upadhyay, K., Sattar, A., Schwanghart, W., McBride, S., Vries, M. V. W. d., Mergili, M., Emmer, A., Deschamps-Berger, C., McDonnell, M., Bhambri, R., Allen, S., Berthier, E., Carrivick, J. L., Clague, J. J., Dokukin, M., Dunning, S. A., Frey, H., Gascoïn, S., Haritashya, U. K., Huggel, C., Kääb, A., Kargel, J. S., Kavanaugh, J. L., Lacroix, P., Petley, D., Rupper, S., Azam, M. F., Cook, S. J., Dimri, A. P., Eriksson, M., Farinotti, D., Fiddes, J., Gnyawali, K. R., Harrison, S., Jha, M., Koppes, M., Kumar, A., Leinss, S., Majeed, U., Mal, S., Muhuri, A., Noetzi, J., Paul, F., Rashid, I., Sain, K., Steiner, J., Ugalde, F., Watson, C. S., and Westoby, M.: A massive rock and ice avalanche caused the 2021 disaster at Chamoli, Indian Himalaya, *science*, 373, 300-306, 10.1126/SCIENCE.ABH4455, 2021.
- 1135 Smith, W. D., Dunning, S. A., Brough, S., Ross, N., and Telling, J.: GERALDINE (Google earth Engine supRaglAciaL Debris INput dEtector) - A new Tool for Identifying and Monitoring Supraglacial Landslide Inputs, *Earth Surf. Dynam. Discuss.*, 2020, 1-21, doi:10.5194/esurf-2020-40, 2020.
- 1140 Su, Z., and Shi, Y.: Response of monsoonal temperate glaciers to global warming since the Little Ice Age, *Quaternary International*, 97-98, 123-131, doi:10.1016/S1040-6182(02)00057-5, 2002.
- van Woerkom, T., Steiner, J. F., Kraaijenbrink, P. D. A., Miles, E. S., and Immerzeel, W. W.: Sediment supply from lateral moraines to a debris-covered glacier in the Himalaya, *Earth Surf. Dynam.*, 7, 411-427, doi:10.5194/esurf-7-411-2019, 2019.
- 1145 Wang, P., Li, Z., Li, H., Wang, W., Wu, L., Zhang, H., Huai, B., and Wang, L.: Recent Evolution in Extent, Thickness, and Velocity of Haxilegen Glacier No. 51, Kuytun River Basin, Eastern Tianshan Mountains, *arctic antarctic and alpine research*, 48, 241-252, doi:10.1657/AAAR0014-079, 2016.
- Williams, H. B., and Koppes, M. N.: A comparison of glacial and paraglacial denudation responses to rapid glacial retreat, *Annals of Glaciology*, 60, 151-164, doi:10.1017/aog.2020.1, 2020.
- 1150 Xu, Q., Shang, Y., AschTheo, v., Wang, S., Zhang, Z., and Dong, X.: Observations from the large, rapid Yigong rock slide – debris avalanche, southeast Tibet, *canadian geotechnical journal*, 49, 589-606, doi:10.1139/T2012-021, 2012.
- Xu, X., Ma, D., He, D., and Huang, H.: Analysis on hydro-thermal combination of debris flow occurrence in Mt. Gongga region, *Mountain Research*, 431-437, 2007.
- 1155 Yao, T., Xue, Y., Chen, D., Chen, F., Thompson, L., Cui, P., Koike, T., Lau, W. K. M., Lettenmaier, D., Mosbrugger, V., Zhang, R., Xu, B., Dozier, J., Gillespie, T., Gu, Y., Kang, S., Piao, S., Sugimoto, S., Ueno, K., Wang, L., Wang, W., Zhang, F., Sheng, Y., Guo, W., Ailikun, Yang, X., Ma, Y., Shen, S. S. P., Su, Z., Chen, F., Liang, S., Liu, Y., Singh, V. P., Yang, K., Yang, D., Zhao, X., Qian, Y., Zhang, Y., and Li, Q.: Recent Third Pole's Rapid Warming Accompanies Cryospheric Melt and Water Cycle Intensification and Interactions between Monsoon and Environment: Multidisciplinary Approach with Observations, Modeling, and Analysis, *Bulletin of the American Meteorological Society*, 100, 423-444, doi:10.1175/BAMS-D-17-0057.1, 2019a.
- 1160 Yao, T., Yu, W., Wu, G., Xu, B., Yang, W., Zhao, H., Wang, W., Li, S., Wang, N., Li, Z., Liu, S., and You, C.: Glacier anomalies and relevant disaster risks on the Tibetan Plateau and surroundings, *chinese science bulletin*, 64, 2770-2782, doi:10.1360/TB-2019-0246, 2019b.
- Yao, X., Liu, S., Sun, M., and Zhang, X.: Study on the glacial lake outburst flood events in Tibet since the 20th Century, *Journal of Natural Resources*, 29, 1377-1390, 2014.
- 1165 Zhang, W.: Some features of the surge glacier in the Mt. Namjagbarwa, *Mountain Research*, 3, 234-238, 1985.
- Zhang, Y., Fujita, K., Liu, S., Liu, Q., and Wang, X.: Multi-decadal ice-velocity and elevation changes of a monsoonal maritime glacier: Hailuogou glacier, China, *journal of glaciology*, 56, 65-74, doi:10.3189/002214310791190884, 2010.
- Zhu, Z.: On Characteristics of Visitor Flow to Hailuogou Glacier Forest Park in Sichuan, *Journal of Huizhou University*, 35, 66-69+80, 2015.
- 1170



1175

Figure 1: Map showing the location of Mt. Gongga (red star), the background image is from ESRI's world basemap (a), several large glaciers around the peak of Mt. Gongga based on Landsat image (b), and retreating history of HLG since the Little Ice Age based on PlanetScope imagery (c). S1 and S2 are tourist sightsee stands on both side of lateral moraines, and the red star indicates the location of Gongga Mountain Station. Longitudinal (A-A') and transverse (B-B', etc.) lines are set to examine the variation of flow velocities and surface elevations (Fig. 3) of the ice tongue.

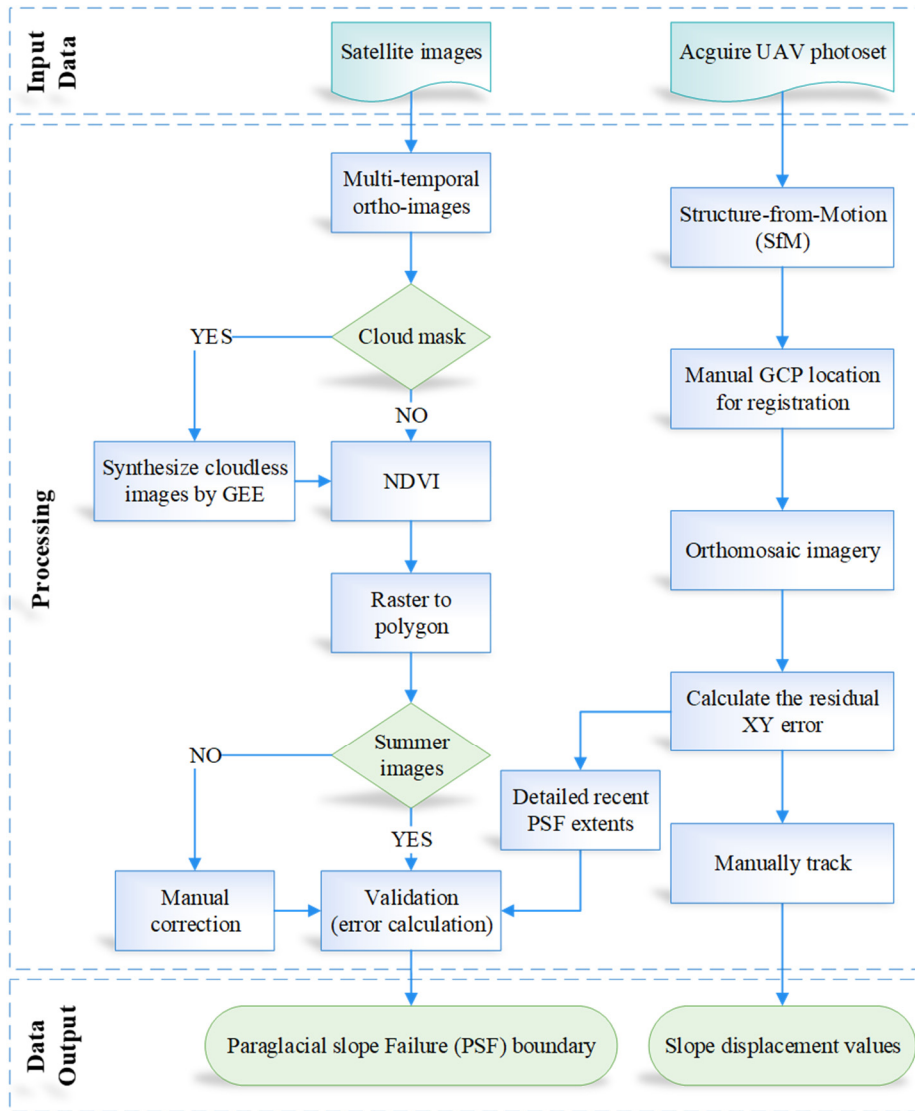
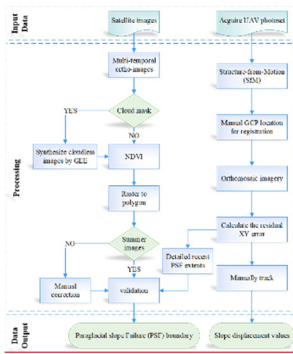
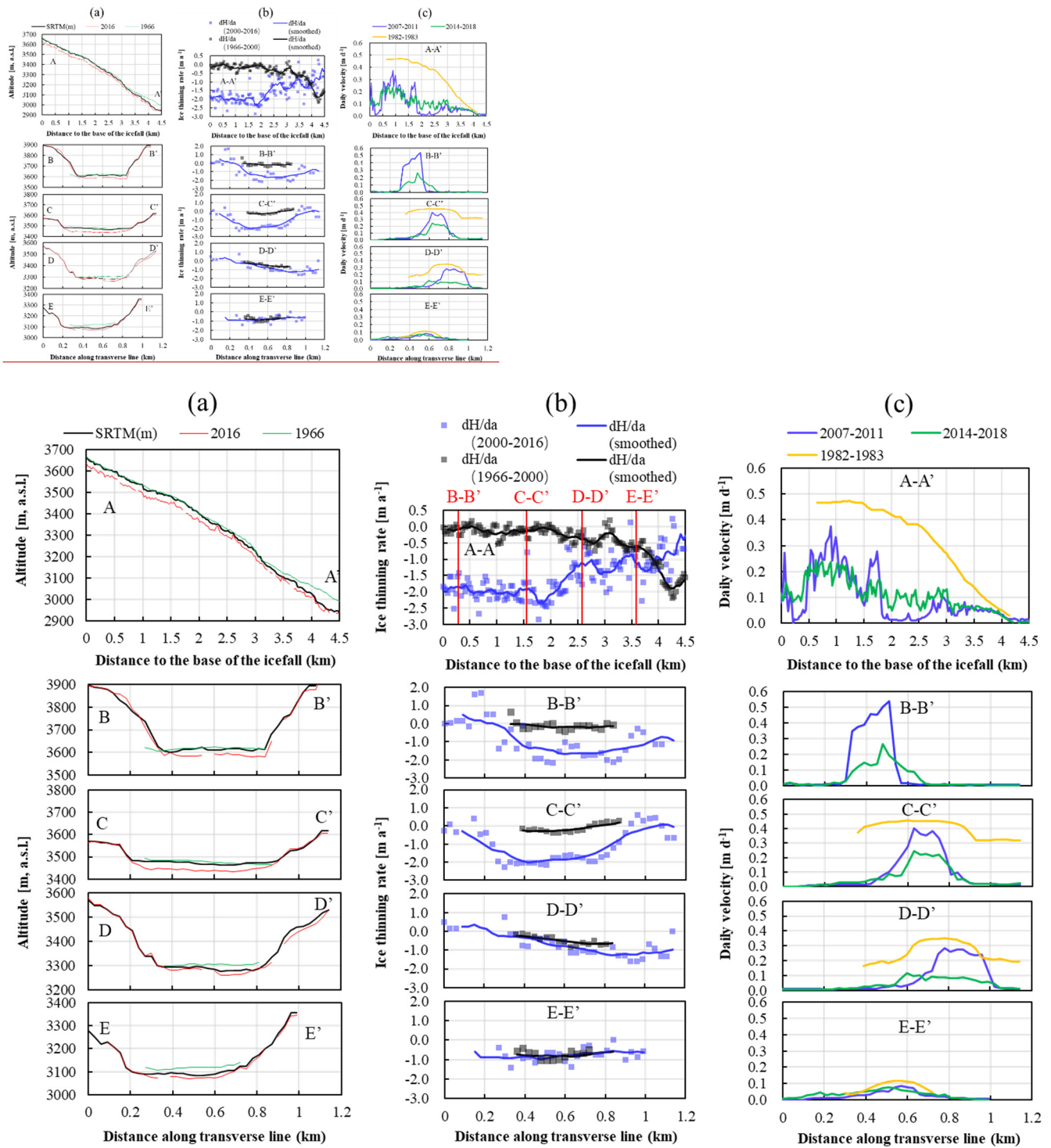


Figure 2: Workflow of the methodology followed to mapping the PSFs (changes) and tracking the displacement from multi-temporal image data.



1185 **Figure 3:** Comparison of ice surface elevations, average annual ice thinning rates (Brun et al., 2017), and velocity changes (Liu et al., 2019a; Zhang et al., 2010) along profiles A-A' to E-E' in Figure 1.

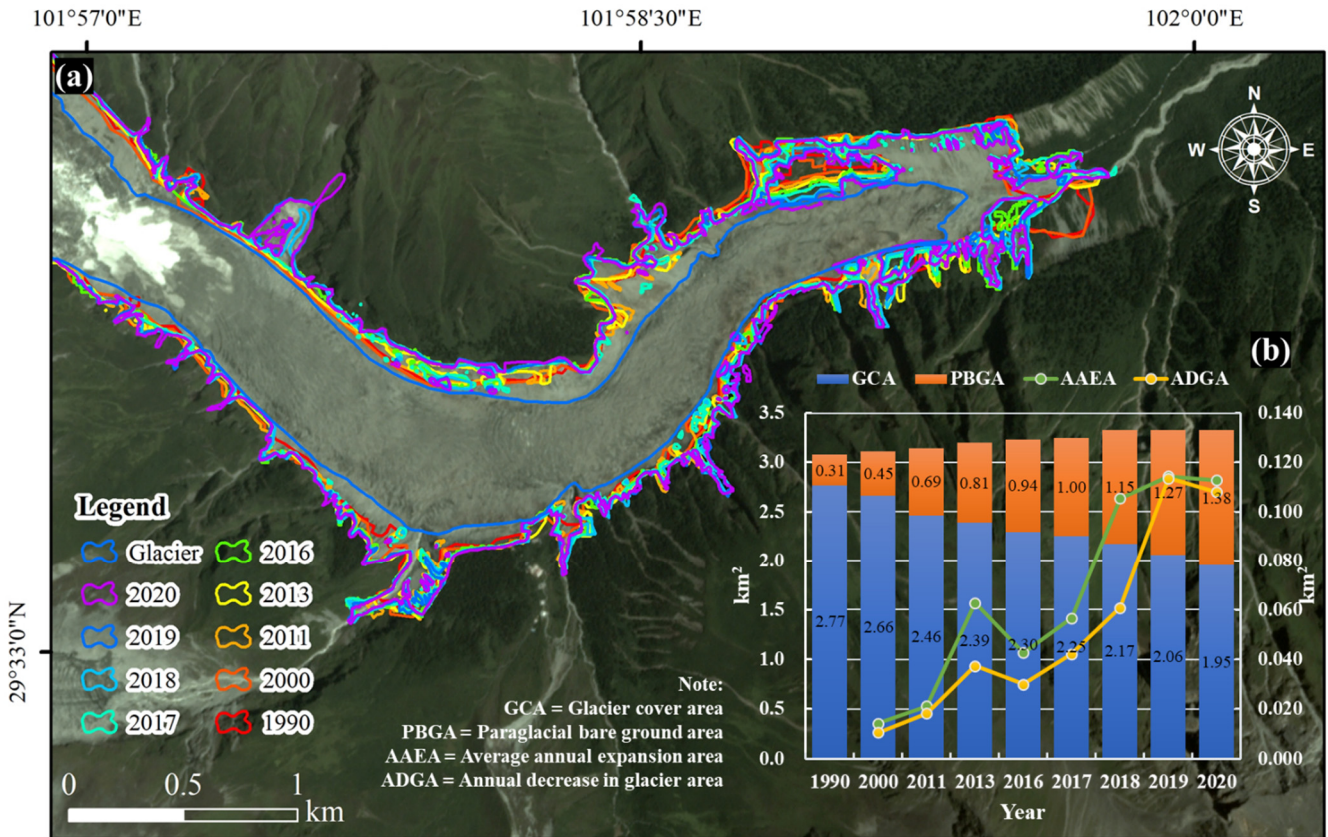
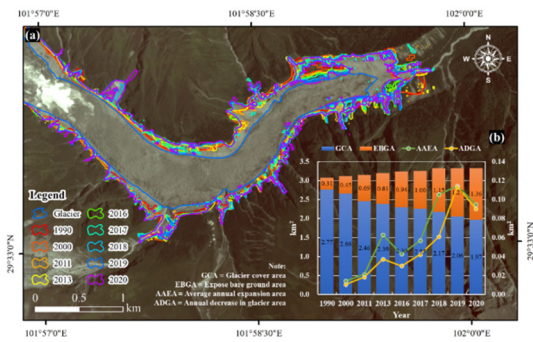
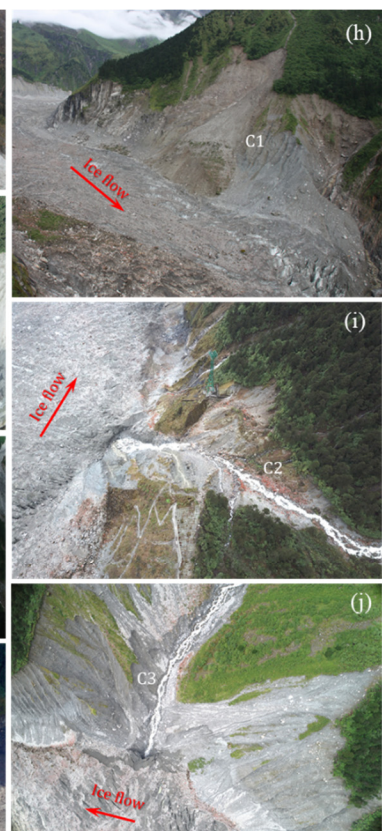
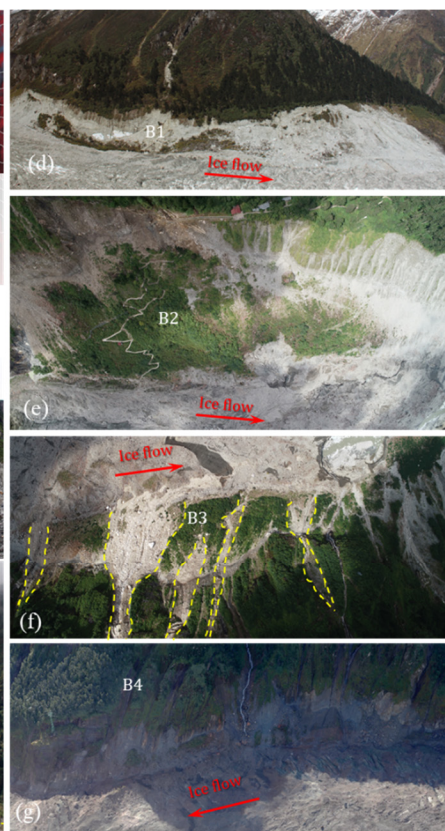
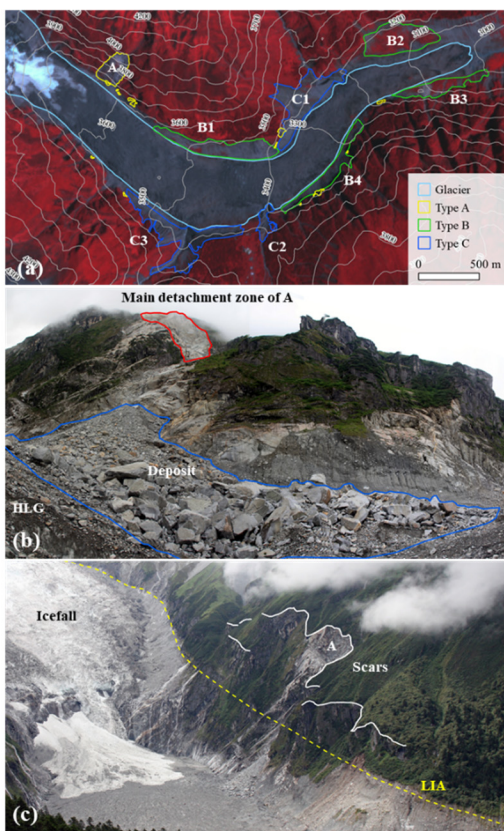
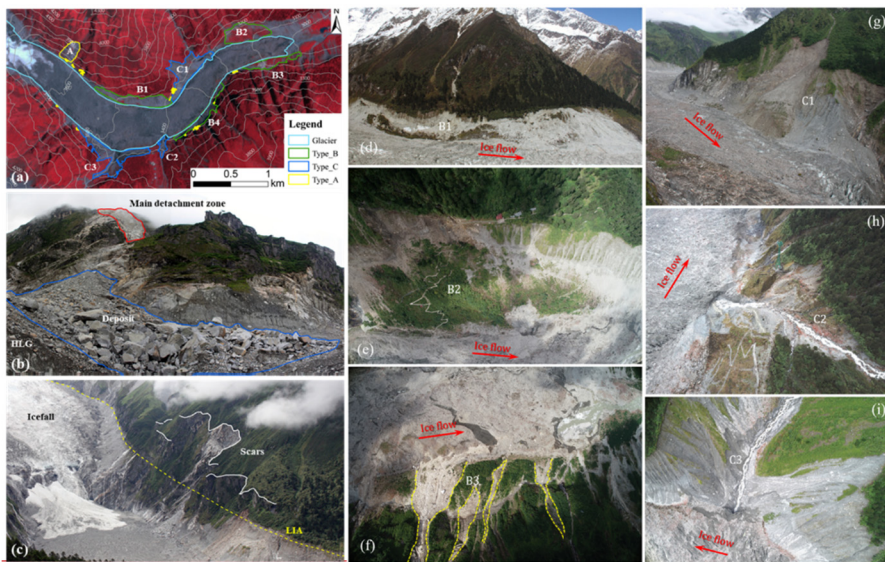


Figure 4: (a) Mapping results of PSFs in the HLG between 1990 and 2020. The glacier boundary (blue line) is mapped by a PlanetScope image acquired on August 16, 2019 (background). (b) Changes of the glacier-cover area (GCA, blue) and the paraglacial bare ground area (PBGA, orange) between 1990 and 2020. The green line indicates the average annual expansion area (AAEA) of PBGA. The yellow line indicates the annual decrease in glacier area (ADGA).

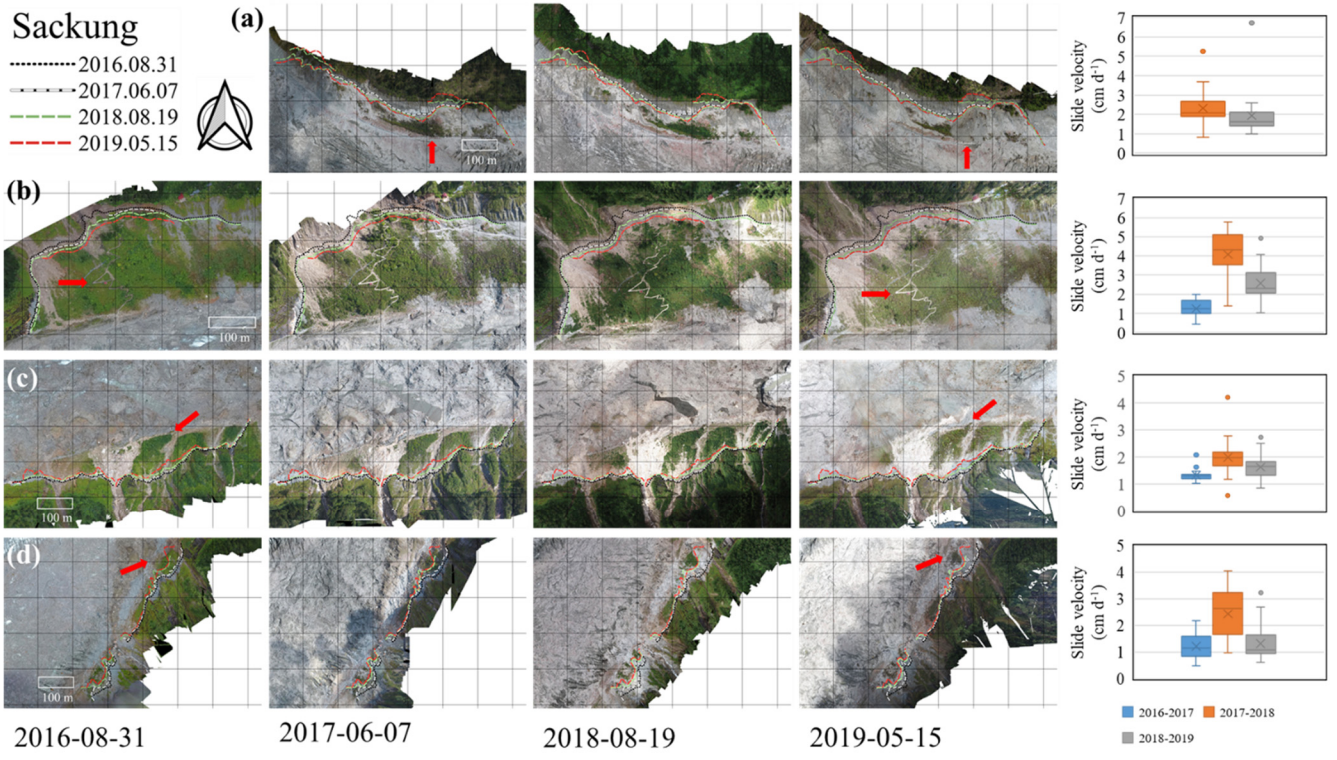
190



195 Figure 5: (a) The distribution of three type of PSFs based on Landsat image. (b-e) The particulars of type A failures in the upper part of the HLG's ice tongue. Main detachment zone (red), Deposit (blue). (c) The scars (white lines) of the surrounding of the rockfall A. Subplots (d, e, f, and g-f) and (g-h, i and j) are closer photographs of Type B and Type C failures, respectively, field photo by Qiao Liu.

Sackung

- 2016.08.31
- 2017.06.07
- 2018.08.19
- 2019.05.15



1200

Figure 6: Slopes slides and its velocity of type B. (a) B1, (b) B2, (c) B3, (d) B4 based on UAV images by Qiao-Liu et al.

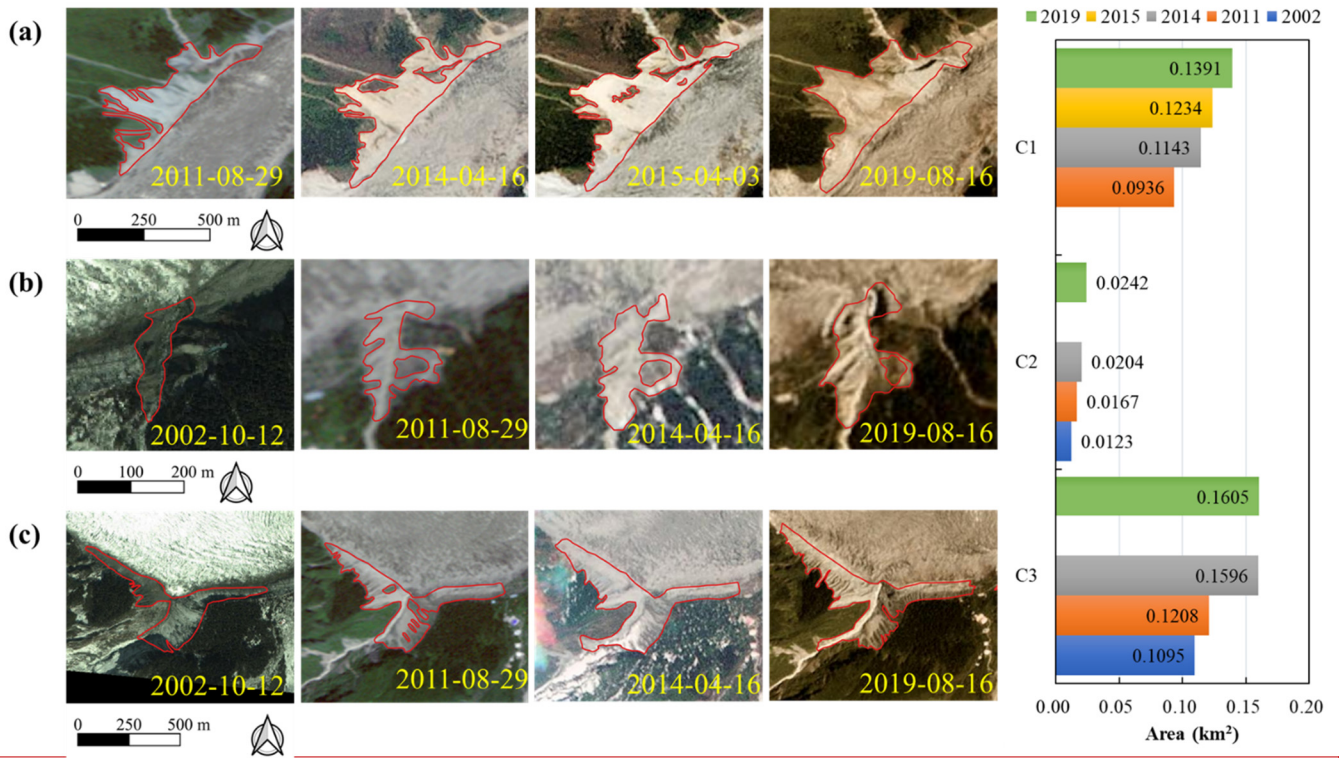


Figure 7: Slopes range and area changes of type C. (a) C1, (b) C2, (c) C3 based on RapidEye, PlanetScope and © Google Earth (SPOT5) images.

1205

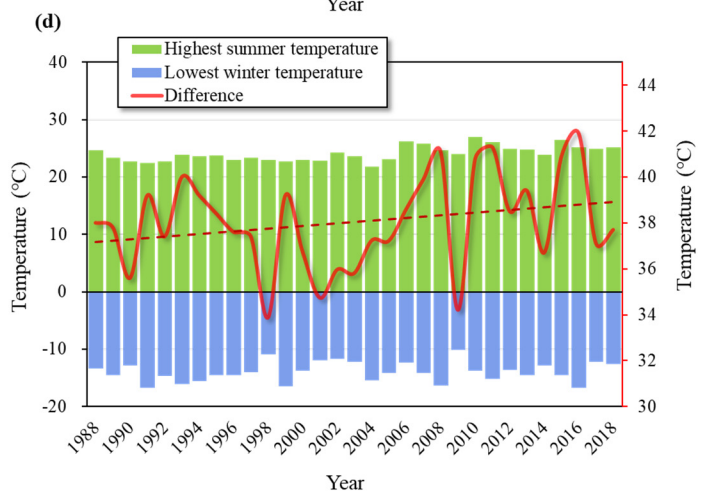
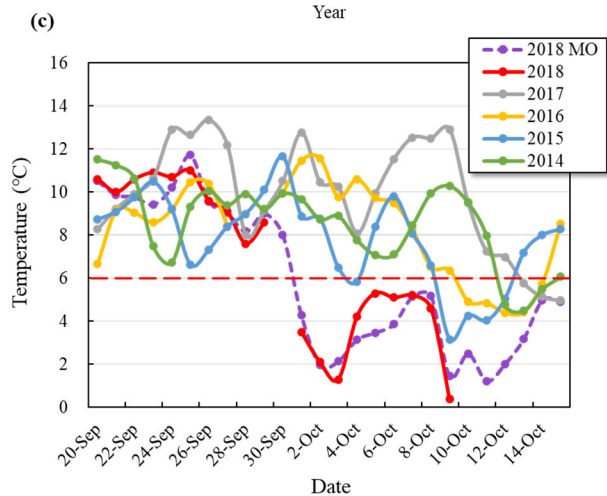
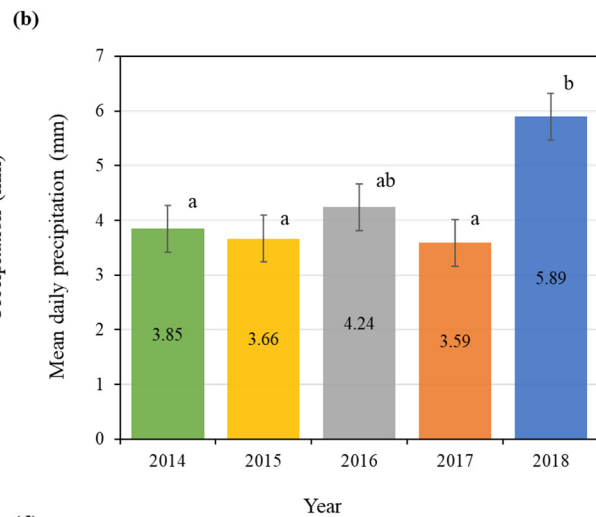
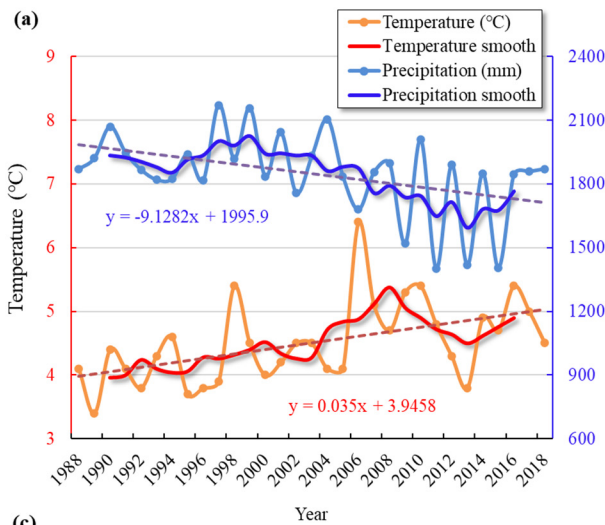
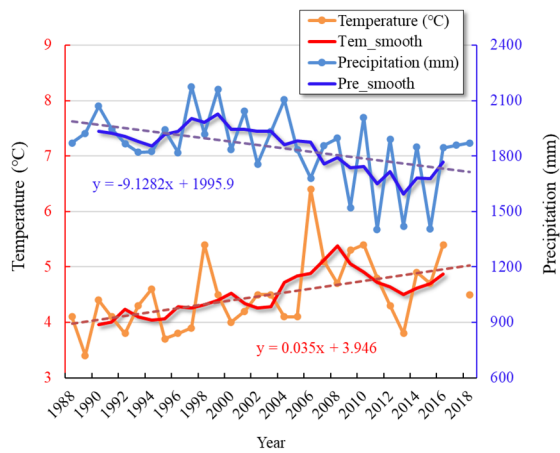
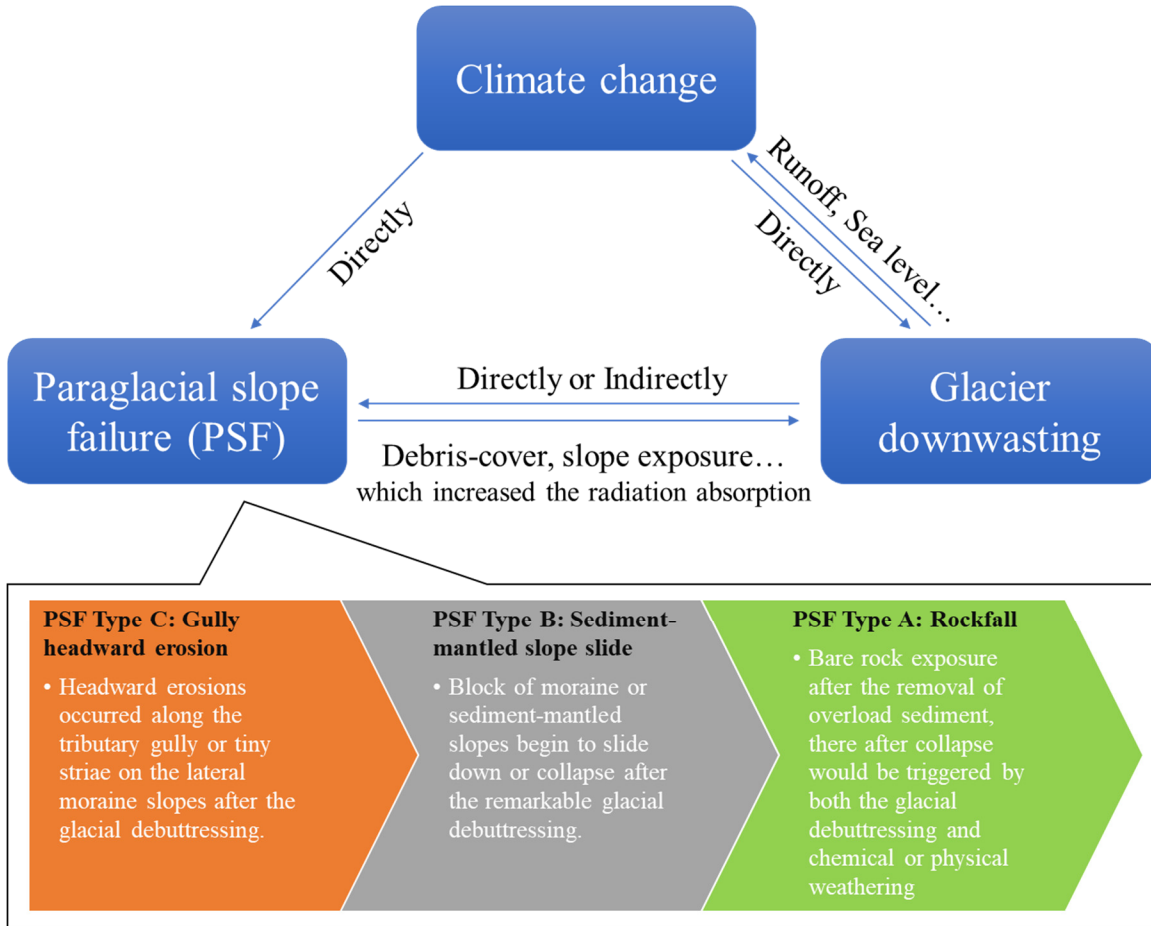
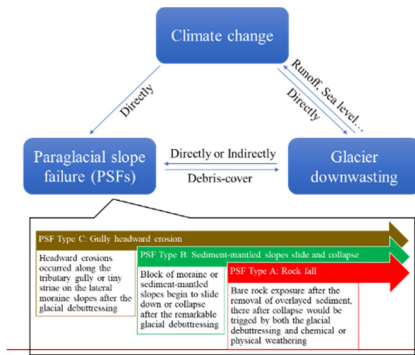


Figure 6: Meteorological data. (a) Mean annual air temperature (orange) and annual precipitation (blue) were recorded at the 3000 m station.

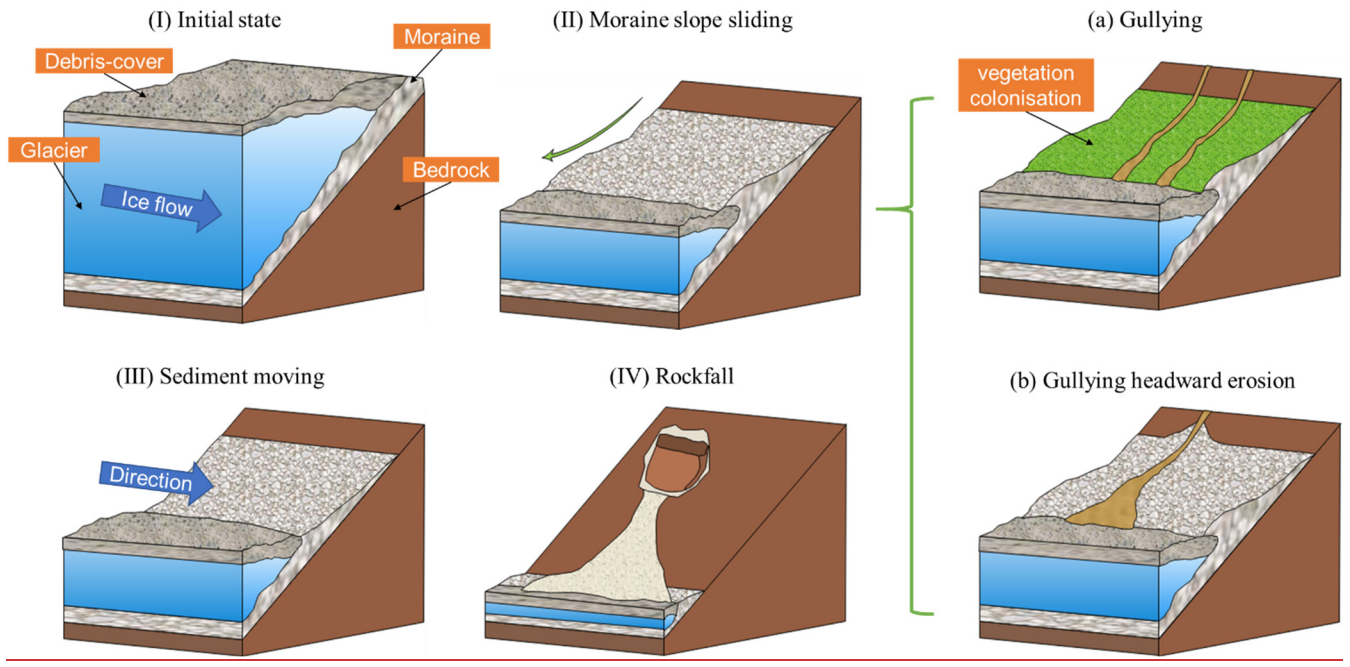
1210 The temperature data for 2017 are from manual observations. Between 1990 and 2016, the moving average for temperature and precipitation has been calculated. (b) Differences in the mean daily precipitation between 5-20 Oct 2018 and 5-20 Oct 2014-2017. Analysis of Variance (ANOVA) was used to investigate the difference of mean daily precipitation between five years, it found that mean daily precipitation in 2018 was significantly higher than that in 2014, 2015, and 2017 ($p < 0.05$). (c) Differences in the daily mean temperature between September to October 2018 and September to October 2014-2017, MO means manual observation. (d) The average of the highest summer temperature (green bar) and lowest winter temperature (blue bar) of each year, and their differences (red line).

1215



1220 **Figure 78:** The relationship among PSFs, ongoing climate change, and glacier downwasting. Climate change can directly trigger the PSF through extreme precipitation and sudden increase/decrease of temperature, or indirectly trigger the PSF by glacier downwasting, which can also be used as a preparatory factor to indirectly trigger PSF (e.g., rockfalls). At the same time, many debris fell into the glacier surface, increasing the range and thickness of the supraglacial debris-cover, which in turn affected the surface energy balance for melting and therefore downwasting rate of the glacier, which will thus influence the rate of runoff generation and its contribution to the sea level rise from glacierised catchments.

1225



1230 **Figure 8: A conjectural model of paraglacial slope evolution and sediment delivery.**

Table 1: Satellite/UAV data used to map the PSFs extents

Sensor Type	Acquiring Date (YYYY.MM.DD)	Near Infrared (NIR)	Red (R)	Spatial Resolution (m)
Landsat TM	1990.07.08/2000.08.20	Band4	Band3	30
Sentinel 2	2016.05.05/2018.08.23	Band8	Band4	10
RapidEye	2011.08.29/2013.05.26/2014.04.16/2015.04.03	Band5	Band3	5
PlanetScope	2017.07.17/2019.08.16/2020.08.20	Band4	Band3	3.125
Google Earth	2002.10.12 (SPOT5)	Band3	Band2	2.5
DJ-UAV	2016.08.31/2017.06.07/2018.08.19/2019.05.15	-	-	0.1

Table 2: Dimensions of PSFs in the study area. We selected periods of high-resolution images with the most obvious terrain changes, the PlanetScope image (2019) for Type A, the UAV images (2016-2019, Fig. S1) for Type B, the PlanetScope, RapidEye, and Google Earth images (2002, 2011, 2014, 2015, 2019) for Type C (locations are shown in Fig. 5a)

1235

PSFs type ID	Length (m)	Width (m)	Area (m ²)	Displacement speed / Upper edge retreat rate (cm d ⁻¹)	Increase in exposed area (m ²)
A	200	283	47,000	-	-
B1	1035	114	112,424	1.96±0.04/-	12,125 (2016-2019)
B2	644	262	122,738	2.63±0.04/-	7,414 (2016-2019)
B3	805	132	63,241	1.65±0.04/-	8,528 (2016-2019)
B4	993	103	73,270	1.66±0.04/-	10,130 (2016-2019)
C1	849	312	139,135	-/3.39±0.20	45,499 (2011-2019)
C2	164	269	24,248	-/0.76±0.11	11,923 (2002-2019)
C3	1097	512	160,474	-/1.15±0.15	50,989 (2002-2019)

Table 3: Precipitation data from 2014 to 2018

	Days (Precipitation >0mm)	Days (Precipitation >20mm)	Days (Precipitation >40mm)	Days (Precipitation >60mm)
2014	302	21	0	0
2015	245	15	0	0
2016	271	25	3	0
2017	278	21	1	0
2018	269	19	2	1